Czech Technical University in Prague
Faculty of civil engineering
Department of concrete and masonry structures

Response of Concrete Structures to Loading by Confined Explosions of Condensed Charges

Author:
Bc. Matyáš Ratislav

A master's thesis submitted to
the Faculty of Civil Engineering, Czech Technical University
in Prague, in partial fulfilment of the requirements for the
degree of Master of Science.

Master's degree study programme: Civil Engineering

Prague, January 2024

Title of the thesis:
Response of Concrete Structures to Loading
by Confined Explosions of Condensed Charges

Student:
Bc. Matyáš Ratislav
E-mail: matyas.ratislav@fsv.cvut.cz

Supervisor:
prof. Ing. Petr Štemberk, Ph.D., D.Eng.
E-mail: stemberk@fsv.cvut.cz
Department of Concrete and Masonry Structures
Faculty of Civil Engineering
Czech Technical University in Prague
Thákurova 2077/7
166 29 Praha 6
Czech Republic

ZADÁNÍ DIPLOMOVÉ PRÁCE

I. OSOBNÍ A STUDIJNÍ ÚDAJE

Příjmení: **Ratislav** Jméno: **Matyáš** Osobní číslo: **486148**

Fakulta/ústav: **Fakulta stavební**

Zadávající katedra/ústav: **Katedra betonových a zděných konstrukcí**

Studijní program: **Stavební inženýrství**

Studijní obor: **Konstrukce pozemních staveb**

II. ÚDAJE K DIPLOMOVÉ PRÁCI

Název diplomové práce:

Odezva betonových konstrukcí na zatížení od vnitřních explozí kondenzovaných výbušnin

Název diplomové práce anglicky:

Response of Concrete Structures to Loading by Confined Explosions of Condensed Charges

Pokyny pro vypracování:

- odezva na zatížení od blízkého výbuchu
- zatížení od tlakové vlny vnitřního výbuchu
- tlaky plynů od vnitřního výbuchu
- odezva betonové konstrukce na rázové zatížení od výbuchu
- aplikace na konkrétním příkladu

Seznam doporučené literatury:

Příručka protivýbuchové ochrany staveb - Daniel Makovička et al.
Calculation of blast loads for application to structural components. - Karlos Vasilis et al.
UFC 3-340-02 Structures to Resist the Effects of Accidental Explosions - U.S. Army Corps of Engineers
Nureg/CR-0442: Effects of air blast on power plant structures and components - Kot C.A. et al.

Jméno a pracoviště vedoucí(ho) diplomové práce:

prof. Ing. Petr Štemberk, Ph.D., D.Eng. katedra betonových a zděných konstrukcí FSv

Jméno a pracoviště druhé(ho) vedoucí(ho) nebo konzultanta(ky) diplomové práce:

Datum zadání diplomové práce: **02.10.2023** Termín odevzdání diplomové práce: **08.01.2024**

Platnost zadání diplomové práce: [redacted]

prof. Ing. Petr Štemberk, Ph.D., D.Eng.	doc. Ing. Lukáš Vráblík, Ph.D.	prof. Ing. Jiří Máca, CSc.
podpis vedoucí(ho) práce	podpis vedoucí(ho) ústavu/katedry	podpis děkana(ky)

III. PŘEVZETÍ ZADÁNÍ

Diplomant bere na vědomí, že je povinen vypracovat diplomovou práci samostatně, bez cizí pomoci, s výjimkou poskytnutých konzultací. Seznam použité literatury, jiných pramenů a jmen konzultantů je třeba uvést v diplomové práci.

Datum převzetí zadání

[redacted]

Podpis studenta

Declaration

Author:

Bc. Matyáš Ratislav

Title of the thesis:

Response of Concrete Structures to Loading
by Confined Explosions of Condensed Charges

I declare that this thesis was composed by myself, that the work contained herein is my own except where explicitly stated otherwise in the text, and that this work has not been submitted for any other degree or processional qualification except as specified.

In Prague …….

…….

Bc. Matyáš Ratislav

Acknowledgement

I would like to express my deepest gratitude to my academic supervisor prof. Ing. Petr Štemberk, Ph.D., D.Eng., as this thesis would not have been possible without his counsel. His facilitative, thought-provoking questions were not only crucial in guiding me through the subject of this thesis, but they also help me to improve my critical thinking in the field of civil engineering in general.

I am also thankful to Ing. Michaela Frantová, Ph.D., for her advice and assistance in addressing the formal requirements associated with the thesis.

Last but not least, I would like to thanks to my family, especially my parents and my partner Kateřina, for their unwavering support throughout my academic journey, even in challenging times.

Abstract

The objective of this master's thesis is to apply and, if necessary, extend existing methods for the calculation of loads caused by close-in and confined explosions. In addition, this work aims to evaluate the structural response of concrete structures subjected to these loads.

The prefatory section of this thesis provides a brief theoretical background on explosives, blast loads, and their effects on concrete structures. The main part of the work is devoted to the evaluation of these loads and the responses of structures to them. Specifically, it focuses on the programmed calculation of the consequences of close-in explosions, the effects of fragmentation of frangible elements, and the evaluation of gas pressures in confined spaces with multiple openings. Furthermore, a straightforward approach for evaluating the response of slab structures to blast loading is presented. These methods are applied to a complex case study.

Keywords: close-in explosion, confined explosion, concrete, frangible element, gas pressure, response to impulse

Abstrakt

Záměrem této diplomové práce je aplikovat a v případě potřeby rozšířit metody pro výpočet zatížení způsobených blízkými výbuchy a explozemi ve vnitřních prostorech. Tato práce se také zaměřuje na predikci strukturální odezvy betonových konstrukcí vystavených těmto typům zatížení.

Úvodní část této práce předkládá stručný teoretický základ v souvislosti s výbušninami, zatíženími výbuchem a jejich vlivem na betonové konstrukce. Hlavní část této práce je věnována metodám vyčíslení těchto zatížení a odezvy na ně. Konkrétně se zaměřuje na programování výpočtu blízkého výbuchu, efektu tříštění fragmentujících prvků a stanovení tlaků plynu v uzavřených prostorech s více otvory. Také je představena zjednodušená metoda pro stanovení odezvy betonových deskových konstrukcí na zatížení výbuchem. Zmíněné metody jsou aplikovány na komplexním příkladu.

Klíčová slova: blízký výbuch, výbuch v uzavřeném prostoru, beton, fragmentující prvek, tlaky plynu, odezva na impulz

Contents

List of Figures

List of Symbols

Latin

A_{av}	Additional venting area
A_f	Area of the deformed frangible element section (including A_{av})
A_{f0}	Original area of the frangible element section
a_{sy2}	Cross-sectional area of tensile reinforcement per unit width
$c_{r\alpha}$	Reflection coefficient
F	External loading force
f	External surface load
f_{sw}	Multiplication factor considering secondary shock waves
H	Cross-sectional dimension of the confinement structure
h	Normal distance of the charge to the nearest reflecting surface
i_g	Gas impulse
i_s	Positive incident impulse
i_T	Total positive reflected impulse
$\overline{i_r}$	Simplified reflected impulse averaged over a given surface
$i_{r\alpha}$	Positive reflected impulse
k_f	Fragmentation coefficient
$\bar{k}_f$	Average fragmentation coefficient
L	Cross-sectional dimension of the confinement structure
l	Normal distance of the charge to the nearest reflecting surface
M	Bending moment
m	Mass
N	Number of adjacent surfaces
P	Overpressure
$\overline{P_r}$	Simplified peak reflected pressure averaged over a given surface
$P_{r\alpha}$	Peak positive reflected pressure
P_{so}	Peak incident overpressure
R	Standoff distance from explosion
S	Restoring force
t	Time
t_A	Time of arrival
u	Displacement / deflection in the centre of a structure

$\dot{u}$	Velocity
$\ddot{u}$	Acceleration
V_f	Free air volume
W	Effective charge weight
W_{EXP}	Charge weight
W_g	Effective charge weight for gas pressures
x	Distance
x_r	Radius of circular wall section
$x_{r,\delta max}$	Value of x_r corresponding to maximal deflection
$x_{r,\theta max}$	Value of x_r corresponding to maximal rotation
y	Normal distance from the point of explosion
Z	Scaled distance

Greek

α	Angle of incidence
ε_{c1}	Maximal concrete compression strain
$\rho_{A,f}$	Area density of the frangible element

Indices

$\cdot_{cp}$	Indexed property related to the control point
$\cdot_{fic}$	Fictitious indexed property
$\cdot_{lim}$	Limiting value of an indexed property
$\cdot_{max}$	Maximum indexed property value
$\cdot_{step}$	Calculation step size of an indexed property
$\cdot_{with}$	Property calculated for a case with a frangible element
$\cdot_{without}$	Property calculated for a case without a frangible element

1 Introduction

The conflict that has persisted in Ukraine over the past two years and the outbreak of the Israel-Hamas war in October 2023 serve as a reminder of the critical need for building designs that ensure the reliability of structures within the crisis infrastructure under extraordinary conditions, such as blast loads. Engineering structures, that lack the ability to withstand these types of loads, can go through irreversible deformation, rendering them unusable, or they can even fail under the extreme loads generated by blast events.

The initial motivation, for researching the topic of this thesis, came from a tragic incident that occurred in the early days of the Russian invasion of Ukraine. Specifically, on 26th February 2022, a missile struck a residential building located on Lobanovsky Avenue in the southwest outskirts of Kyiv, which caused the destruction of six apartments and damaged the load-bearing structures on several floors [1]. The origin of the missile has not yet been officially disclosed. The state-owned Russian news agency TASS alleged that the missile in question was of Ukrainian origin, as an anti-aircraft weapon, yet these claims were disputed by Ukrainian sources [2][3]. The distinction between truth and falsehood has gained increasing significance in modern times. In the field of civil engineering, this distinction can be achieved through simple calculations or engineering estimates. Proficiency in conducting rapid indicative calculations of structural responses to blast loading and the ability to use them appropriately are valuable not only for fact-checking, but also for the preliminary design of protective structures, containment facilities, or crisis infrastructure buildings. The engineering estimates derived from such calculations can also serve in evaluating the condition of buildings damaged by various incidents.

This thesis focuses on the loads generated by non-contact high explosives explosions in confined spaces and their effects on concrete structures. It evaluates these loads and associated responses from two distinct viewpoints: one focused on the local response to the primary blast wave, and the other focused on the global response of the entire structure subjected to primary and reflected waves, and gas pressures. In both approaches, the analysis is restricted to the positive phase of the blast wave. This thesis focuses more on the effects that are not sufficiently described in the available literature – more on that in the Chapter 3 – Goals.

This paper draws on a range of English and Czech literature. Of particular relevance to this thesis are two publications - NUREG/CR-0442 and UFC-3-340-02. These two publications outline methods for calculating problems within the scope of this thesis. These methods were employed in this thesis to address a practical scenario and were extended if deemed appropriate.

This thesis is structured as follows: Chapter 2 introduces the theory behind explosives, including the air pressures they generate when detonated and how these pressures interact with structures. The response of these structures to explosive loads is also described. Chapter 3 then establishes the objectives of this thesis. Chapter 4 is the practical section of this thesis, which outlines methods for calculating the response of concrete structures to blast loads caused by close-in and confined explosions. A specific case study demonstrates the application of these methods. Chapter 5 summarizes the main discoveries of this thesis.

2 Blast Dynamics and Structural Response

This chapter introduces the state of the art in the subject matter of this thesis. It is crucial to have an understanding of the theory behind the formation and propagation of blast waves, and their interactions with obstacles in order to make engineering decisions in the practical part of this thesis. This chapter is structured chronologically in relation to the detonation process and its aftermath. The explosives are described first, followed by a description of the pressures they generate in the air. Subsequently, the interactions of these pressures with structures are considered, and finally, the last chapter of this part of the thesis is devoted to the response of structures to the loading.

2.1 Explosions and Explosives Characteristics

Explosions are classified based on the types of explosives from which they originate. These types and classifications are discussed in the first section of this chapter. Subsequently, the chapter briefly explores the characteristics of explosives, particularly their shapes and effective weight, the former in Section 2.1.2 and the latter in Section 2.1.3.

2.1.1 Types of Explosives and Explosions

An explosion is a phenomenon characterized by the rapid release of energy in the form of heat, increased pressure, and usually light. Objective classifications of explosions are based on the nature and origin of the energy released and they include nuclear, physical, and chemical explosions [4]. In nuclear or atomic explosions, energy is released through the splitting or fusion of atoms. Physical explosions result from an extremely rapid change in the state of a substance, resulting in the generation of pressure, or from the rapid release of positive or negative pressure from a containment [5]. Chemical explosions, on the other hand, stem from exothermic chemical reactions and oxidation [6]. This thesis is focused on chemical explosions.

Chemical explosions may be caused by explosives in various forms: condensed explosives, clouds of gas or vapour, and dispersed dust. Condensed explosives are materials that release large amounts of energy rapidly through a chemical reaction independent of their environment (for example a TNT explosive). In contrast, gas or vapour clouds and dust dispersions use air as their

oxidising agent. Both types rely significantly on the fuel type and its concentration in air. Explosions of dust dispersions, including for example wood dust particles smaller than 0.5 mm, occur solely in enclosed spaces. However, gas or vapor cloud explosions can form even outdoors, for instance, in a form of petrol leakage. [4][7] This thesis devotes oneself to condensed explosives.

Explosive substances can be classified into high explosives and low explosives. In the case of low explosives, fuel and an oxidizer are mixed together. Upon ignition, heat is propagated through the explosive, causing deflagration, where the oxidiser and fuel react together to produce hot gas. Common examples of low explosives are gunpowder and ammonium nitrate explosives. High explosives, conversely, contain a solitary reactant, where the fuel and oxidiser are mixed on a molecular level. Upon initiating the chemical reaction, the reactant molecules decompose, and the charge detonates. The reaction in high explosives is faster (detonation velocities are often between 6,000 and 9,000 m/s) than in low explosives, but they are often less sensitive to heat for initiation. Consequently, they are categorised into either primary or secondary high explosives. Primary explosives, such as lead azide, are highly sensitive to heat, sparks, and shock and are employed to initiate secondary explosives. Meanwhile, secondary explosives (for example TNT, SEMTEX, or Octol 70/30) are much less sensitive. [6][8]

2.1.2 Shapes of Condensed Explosives

The performance of condensed explosives also depends on the shape and casing of the charge. Semi-empirical methods frequently portray high explosives as spherical for ease of calculation, despite the reality that most explosions involve non-spherical charges, typically cylindrical. In spherical high explosives, the detonation wave theoretically reaches every point of the explosive simultaneously, creating a symmetric blast wave in all directions. The shock wave generated by a cylindrical charge exhibits distinct features, which vary according to the azimuth angle (angle between the measurement axis and the longitudinal axis of the cylinder). [9][10]

The performance of an explosive is also determined by whether it is sealed or not. The casing influences the conditions of the chemical reaction and the propagation of the generated pressure wave, changing its properties. [4] In this thesis, explosions of unsealed spherical explosives are considered.

2.1.3 Effective Charge Weight

As there are numerous explosives with diverse properties, a universal quantity - TNT equivalent W (also known as effective charge weight) - is used for calculations of blast parameters. Effective charge weight is the hypothetical mass of trinitrotoluene, which can generate the same detonation energy as the actual weight of the explosive in use. The conversion factors of commonly used explosives are listed, and the weight W can usually be determined by multiplying the actual charge weight W_{EXP} with the respective conversion factor. [4] [12]

To calculate gas pressures resulting from an explosion in a confined space, the effective charge weight is determined differently. This is because the TNT equivalent of an explosive in terms of gas pressures W_g depends not only on the explosive' heat of detonation but also on its heat of combustion. [11]

2.2 Air Pressures Caused by Explosions

The air pressures resulting from explosive events can be categorized as blast pressures and gas pressures. Section 2.2.1 addresses blast pressures, focusing on time evolution, while Section 2.2.2 delves into their characteristics at a specified distance. Gas pressures are discussed in Section 2.2.3.

2.2.1 Blast Wave Formation and Propagation through Air

Pressure waves generated by explosions can be categorized into two types: continuous waves, which have a gradual increase in pressure (Figure 1: t_1), and shock waves, which have a sudden pressure increase at their front (Figure 1: t_3). After a detonation, a shock wave is created, whereas after a deflagration, a continuous pressure wave is formed. [4]

However, if the continuous wave is strong enough, it can transform into a shock wave. An increase in pressure leads to an increase in temperature. As the speed of sound in air is reliant on the air temperature, the amplitude of the wave - the point with the highest pressure, temperature, and therefore sound speed - reaches the front of the wave. Initially, this front was spreading at the speed of sound in the air ambient conditions. Consequently, at its front, the wave encounters a sudden increase in pressure, creating a shock wave (refer to Figure 1: t_1 to t_3). Therefore, it is necessary for the shockwave to propagate through the

air at a speed higher than the speed of sound in the surrounding environment. [5][13]

The steep pressure and temperature gradient on the wavefront leads to dissipation. Energy losses lead to a decrease in pressure and temperature, which reduces the speed of the wavefront. This process continues until the blast wave transforms into a continuous sound wave. Pressure fluctuations in the wavefront create a blast wind that flows in the same direction as the wave propagates. This phenomenon can produce a zone of negative pressure behind the blast wave. This process is illustrated in Figure 1: t_3 to t_5. [4][5][13]

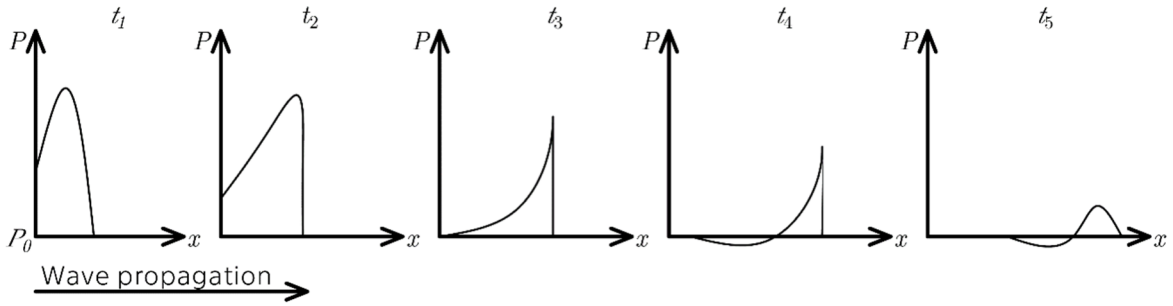

Figure 1: Blast wave formation and propagation through air

2.2.2 Ideal Blast Wave Characteristics

Since real blast waves are very complex and their characteristics are to some extent chaotic, their behaviour is idealised. The characteristics of an ideal blast wave are considered at a given distance from the point of detonation (the centre of the spherical condensed charge) R. The important features of an ideal blast wave can be clearly illustrated in its pressure-time history diagram (Figure 2). This history can be divided into three sections. The time from the detonation until the front reaches the distance R – time of arrival t_A. The positive phase with a duration of t_0 and a peak incident overpressure P_{so}, and a negative phase with a duration of t_0^- and a peak negative incident pressure P_{so}^-. If the pressures of the positive phase are integrated over the phase duration, it results on positive incident impulse i_s, and similarly for the negative phase. For design purposes, the negative phase is usually not considered. For the vast majority of explosives, the main structural damage is caused by the positive phase. In this paper, only the positive phase of the blast wave is considered. [12][14]

The pressure drop of the ideal wave is exponential. Friedlander's equation,

$$P(t) = P_{so}\left(1 - \frac{t}{t_0}\right) e^{-b\frac{t}{t_0}}, \tag{2.1}$$

is widely used to describe this pressure drop if only the positive phase is considered. In this equation t denotes the elapsed time, measured from the instant of blast arrival, and b denotes a decay coefficient that is iteratively solved so that the impulse subtracted from the resulting pressure-time history graph matches the experimental data. [12]

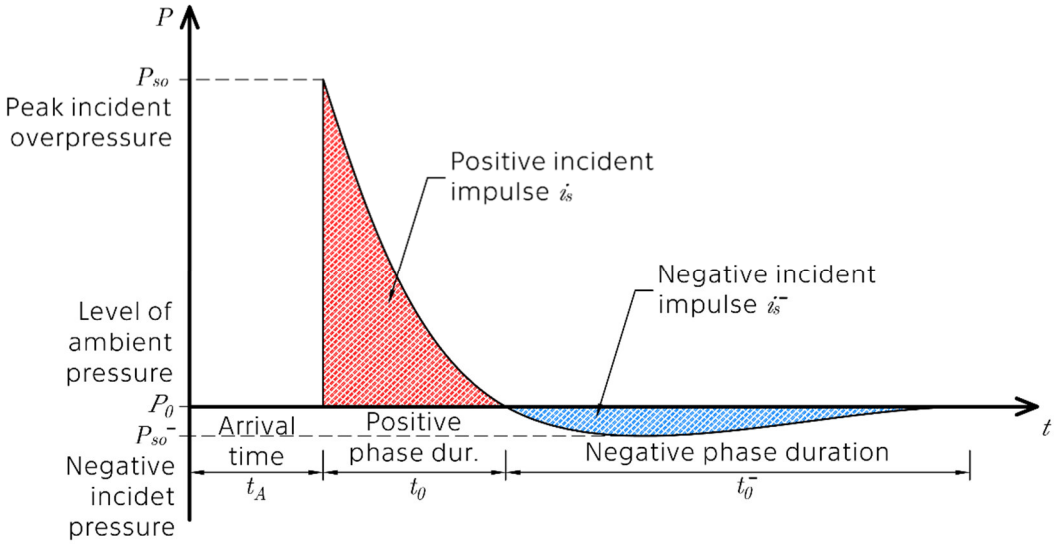

Figure 2: Pressure time history of an ideal blast wave

The pressure time history can be simplified to a triangular form, where there is only a linear dependence of the pressure on the time elapsed. In this case, a fictitious duration of the positive phase $t_{0,fic}$ is calculated based on the following relation:

$$t_{0,fic} = \frac{2\ i_s}{P_{so}}. \tag{2.2}$$

The calculation is based on the equilibrium of the positive incident impulse integrated from the pressure-time graph and the experimental data. [4][11]

An example of a scale comparison between a simplified triangular pressure-time history graph and a graph calculated using the Friedlander's equation can be seen in Figure 3.

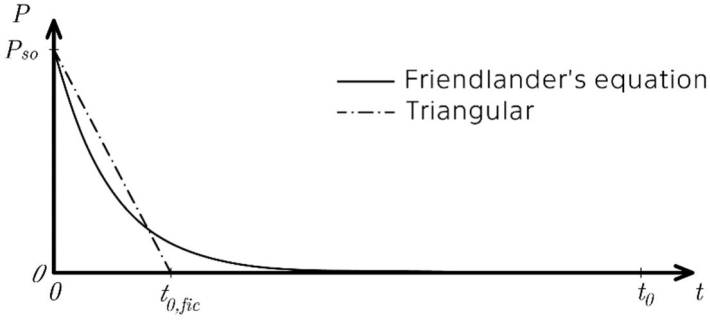

Figure 3: Comparison of pressure-time history graphs of free air blast wave

The blast wave parameters i_s and P_{so} depend on the effective charge weight W and the distance from the explosion R. Due to scaling laws, only one independent variable, the scaled distance Z, can be calculated from these input variables. The cube root scaling rule, also known as the Hopkinson-Cranz scaling,

$$Z = \frac{R}{\sqrt[3]{W}}, \tag{2.3}$$

is widely used to describe the scaled distance Z. [15]

Since blast waves are complex phenomena that depend on conditions that are difficult to define, an empirical approach is used to obtain their characteristics. Several empirical equations can be used, each suitable for different charge types, boundary conditions and ranges of scaled distances. In practice, blast wave parameters can be obtained from diagrams for two basic scenarios: spherical shock wave (free air burst – Figure 4) and hemispherical shock wave (surface burst - beyond the scope of this paper). In these plots, some parameters are scaled by the cube root law. In addition to the previously presented parameters, the diagrams include the shock wave velocity U and the shock wave wavelength L_W. [12]

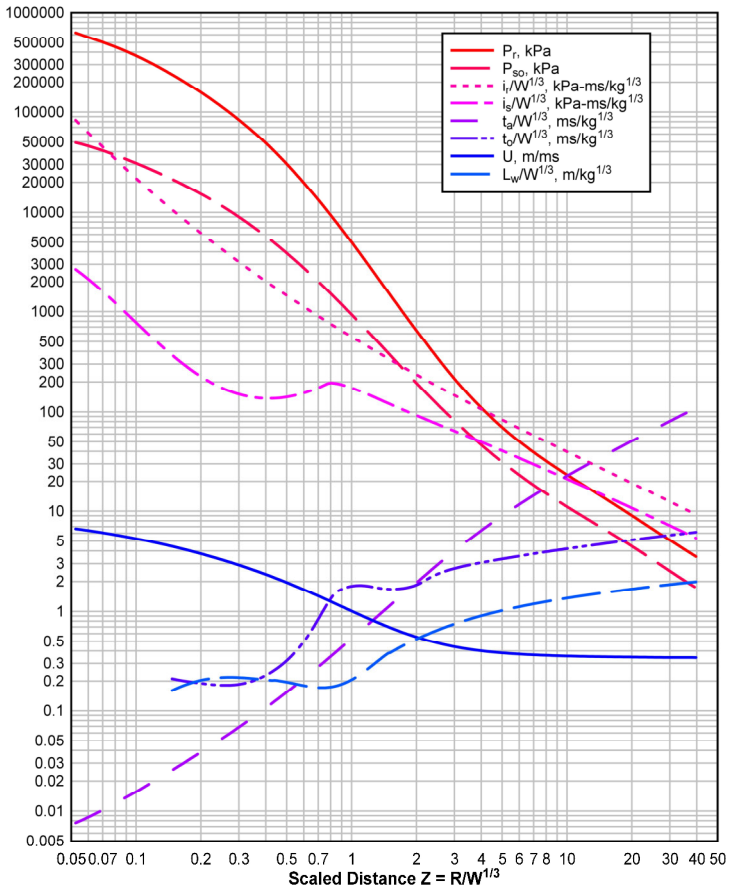

Figure 4: Parameters of positive phase of shock wave from free-air bursts [12]

2.2.3 Gas Pressures

In a confined environment, such as a room or silo with small (or no) openings, when an explosive detonates, the temperature rises, and gaseous products of the explosion are produced. This results in an overpressure in the area behind the blast wave that fills the space. These overpressures are called gas pressures, and they act on surrounding structures as "quasi-static" loads.

The peak gas pressures P_g are generally lower than the pressures at the front of the blast wave. However, the duration of these pressures t_g is significantly longer than the duration of the blast wave t_0 in confined structures. Therefore, the gas impulse i_g can be significant. Both P_g and i_g are dependent on the free volume of the confinement V_f and scaled charge weight W_g. The value of i_g highly depends on the size of the vent openings A_v. If the duration of gas pressures due to venting is shorter than the duration of the blast wave ($t_g/t_0 < 1$), the gas pressures can be neglected, and the structure is considered to be fully vented. Experimental models suggest that, conservatively, a space can be considered fully ventilated if $A_v/{V_f}^{2/3} > 0{,}6$. Time dependence of gas pressures can be simplified to a triangular form, similarly to incident pressures by employing fictitious duration of those pressures. This duration can be obtained from following relation: [11][16]

$$t_g = \frac{2\, i_g}{P_g}. \tag{2.4}$$

2.3 Interactions Between Blast Waves and Structures

The characteristics of loads generated by the blast wave on structures depend on the chosen level of simplification, often determined by the explosion environment. General approach for air blasts is outlined in Sections 2.3.1 and 2.3.2. Section 2.3.3 explores the application of the general methods for close in explosions, while Section 2.3.4 addresses the loads in confined spaces reinforced due to reflections. The final section is dedicated to the interaction of blast waves with elements that fail during the blast loading.

2.3.1 Pressures Acting on Structures

When a shock wave encounters a rigid surface, it is reflected, causing the surface to be loaded by overpressures called reflected overpressures (also

known as reflected pressures) - with peak value $P_{r\alpha}$. These pressures depend on the scaled distance Z (in other words, on the magnitude of the blast wave) and on the angle of incidence α. The angle of incidence and its effects are discussed in Chapter 2.3.2. In this chapter, a normal blast wave incidence on the surface is considered. In this special case, the reflected pressures are called normal reflected overpressures, and their peak value is denoted as P_r.

Normal reflected overpressures are always higher than incident overpressures at the same scaled distance - typically from 2 to more than 12 times higher, depending on peak incident overpressure P_{so}. The reason for this amplification effect is that the air particles propelled by the shock wave collide with the surface. In the ideal linear elastic case, where particles can bounce freely off the surface (common for blast waves with small P_{so}), this results in a doubling of the overpressure acting on the surface. However, for strong blast waves, the air particles reflection is obstructed by other air particles pushed by the blast wave, causing even more amplified loading. [4][12]

The normal reflected overpressure integrated under its pressure-time-history curve is called the normal reflected impulse, denoted as i_r. Both P_r and i_r can be obtained from Figure 4 for a given scaled distance Z. The aforementioned pressure-time curve of the reflected overpressure is compared with the incident pressure history curve of an ideal wave in Figure 5. For design purposes, the time evolution of the pressures can be simplified to a triangular form, by employing fictitious duration of reflected pressures – calculated as $t_r = 2i_r/P_r$. [12]

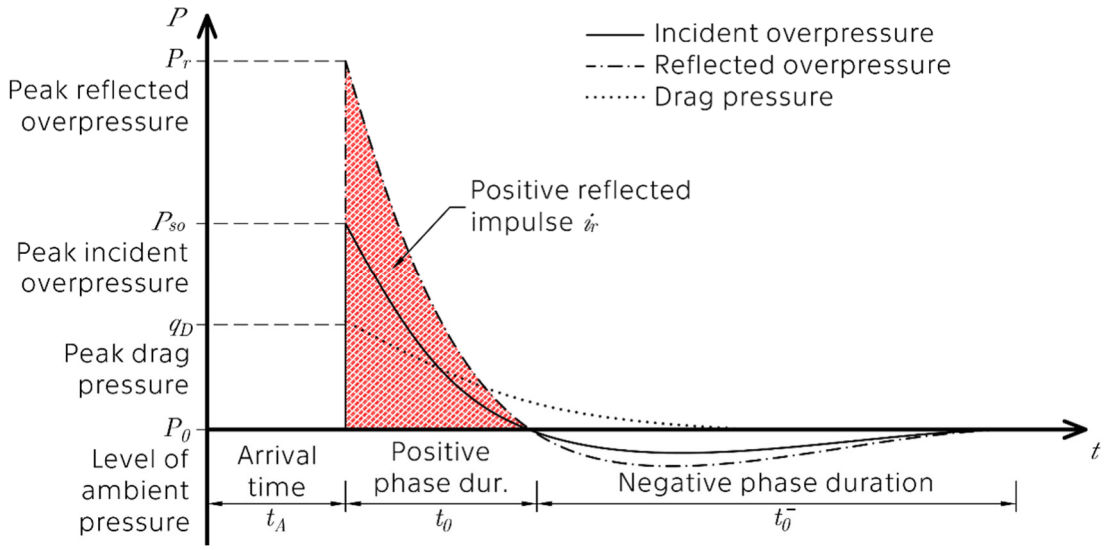

Figure 5: Comparison of incident, reflected and drag pressure time histories

Blast wind (also known as explosion wind) mentioned in Chapter 2.2.1 also loads the surface. The resulting pressure acting on the structure is called drag pressure with an initial peak value q_D. Peak drag pressures are generally smaller than reflected pressures, but they persist for longer periods of time (see Figure 5). The magnitude of q_D depends on the characteristics of the blast wave, namely the peak incident pressure, and the drag coefficient of an object exposed to the wind C_D. [4][12]

The time dependency of the pressures acting on an object varies with its size. There are two primary effects to consider: pressure clearing and pressure summation on the front and rear of the object.

When a blast wave encounters a finite object surface, the reflected pressures generated on the object's front side are reduced by wave leakage around the object. This may lead to a quicker drop in reflected pressure than in the case of an infinite surface. The duration between the peak reflected overpressure to the incident pressure plus dynamic pressure is termed as the clearing time t_c. This duration can be estimated using different empirical equations, which rely on the boundary conditions. These equations commonly take into account the surface dimensions and speed of sound in the wave. If the surface is extensive and the calculated reflected impulse is greater than that of an infinite surface, the method involving the infinite surface is used for further calculations.[4][12]

As the blast wave spreads, it encircles the object and applies load to its sides. Once it reaches the rear wall, the pressure front expands at the edges, creating secondary waves. These waves propagate along the rear surface, gradually imparting a positive load to the surface. To simplify practical calculations, an equivalent uniform load is applied across the entire rear surface. Once the entire rear side is loaded, the load begins to decrease as the incident pressure of the blast wave drops. The loading history of the rear side of an object is subtracted from the loading of the front side since it acts in the opposite direction.

Due to these two effects, small objects only experience a fraction of the shock wave impulse compared to infinite surfaces. The loading history of very small objects is characterised by only a brief initial spike of reflected pressure and drag pressures. Small objects have a short clearing time, which means that the pressure acting on the rear surface of the object is almost simultaneously loaded with reflected pressure equal to the incident overpressure, cancelling the pressures exerted on the front surface of the object. [4][11]

2.3.2 Angle of Incidence and Mach Stem

In the previous chapter, it was noted that the reflected overpressure is reliant on the angle of incidence α. This angle is measured between the normal of the surface and the normal of the blast wave front (so, for the normal blast wave described earlier, $\alpha = 0$). The effect of the angle on reflected pressures can be quantified by the reflection coefficient $c_{r\alpha}$, defined by the expression:

$$c_{r\alpha} = \frac{P_{r\alpha}}{P_{so}}. \tag{2.5}$$

The coefficient value relies on the angle of incidence α and the peak incident overpressure P_{so}. Coefficient $c_{r\alpha}$ can be derived from the graph in Figure 6. [12]

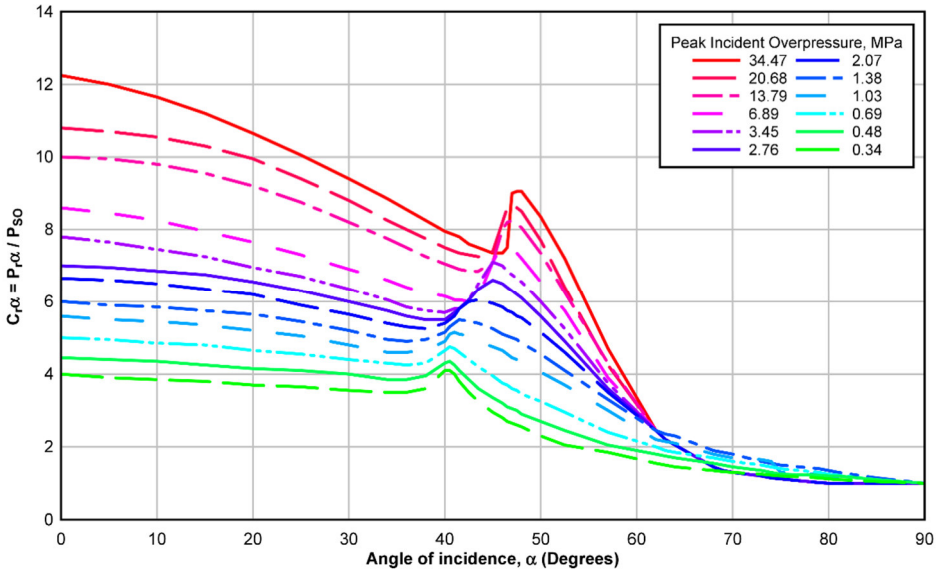

Figure 6: Reflected pressure coefficient to angle of incidence graph [12]

Notice that at an angle of incidence $\alpha = 90°$ in Figure 6, the reflection coefficient is for all P_{so} equal to 1. Therefore, surfaces parallel to the direction of propagation of the blast wave are initially loaded by peak reflected overpressure $P_{r90°} = P_{so}$. From Figure 6, it is also apparent that for angles of incidence $\alpha < 35°$, the value of normal reflected overpressure can be conservatively used for reflected overpressure. However, this statement is not applicable for angles $\alpha \in \langle 40°; 50° \rangle$, particularly for low to moderate peak incident pressures. In this range of angles, a Mach stem occurs, leading to an increase in the reflected pressures. [12]

When a blast wave reflects off a surface, the reflected wave front moves slightly faster than the incident wave. This is because it travels through air that has been heated and compressed moments before by the incident wave. Within

the range of angles of incidence mentioned (40-50°), consequently the reflected wave takes the lead. Subsequently, both fronts combine and create a single shock front, known as a Mach stem (or Mach wave). The location where the incident wave shifts to the Mach stem is known as the triple point. Mach waves act similarly to the regular blast waves previously discussed. Figure 7 illustrates the creation of the Mach stem and its advancement along a rigid surface. [17][18]

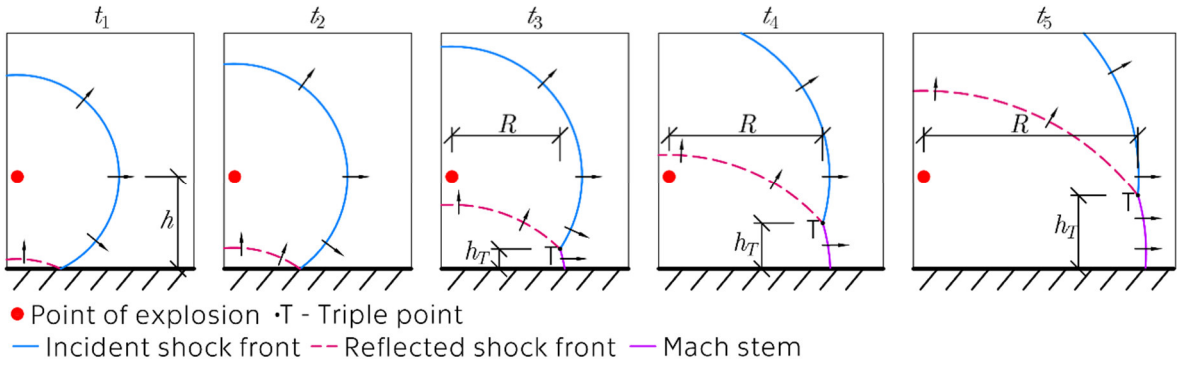

Figure 7: Formation and propagation of a Mach stem along a rigid surface

The height of the triple point h_t can be determined by employing the scaled distance Z and the scaled height of the explosive above the reflective surface $H_c = h \bullet W^{-1/3}$ (refer to Figure 7). The calculation method varies according to specific conditions [12][19]. If $H_c \in \langle 0.215\ ;2\rangle$ and $Z \in \langle 0.2\ ;4\rangle$ both in $[m/kg^{1/3}]$, the scaled height of the triple point $H_t = h_t/W^{1/3}$ can be calculated using the following equation (corrected from [19]):

$$H_t = \left(\frac{0.0012}{{H_c}^4} + \frac{-0.0113}{{H_c}^3} + \frac{0.0466}{{H_c}^2} + \frac{0.0118}{H_c}\right) \cdot \cdot Z^{(-0.7502\ {H_c}^4 + 3.8861\ {H_c}^3 - 5.8343\ {H_c}^2 + 2.4117\ H_c + 2.3112)}. \tag{2.6}$$

2.3.3 Close-in Explosions

Scenarios, in which blast waves are relatively small or comparable in magnitude to the reflecting surface, are commonly referred to as close-in explosions. In such cases, surfaces are often regarded as infinite due to large clearing times (see Chapter 2.3.1). Compared to larger explosions occurring at greater distances, blast loading in close-in explosions is more localized and varies across the surface. This aspect must be considered when calculating close-in explosions.

The process of a wall or slab being subjected to a close-in blast can be visualised as a spherical blast wave (for a spherical charge) propagating over a

surface, loading an increasing circular section of the structure. The reflected overpressures vary for any given radius of the circular section x_r due to the different angles of incidence α and the standoff distances R. The spatial arrangement is shown in Figure 8. For structural response calculations, it is typically assumed that the complete circular area is loaded simultaneously. [20]

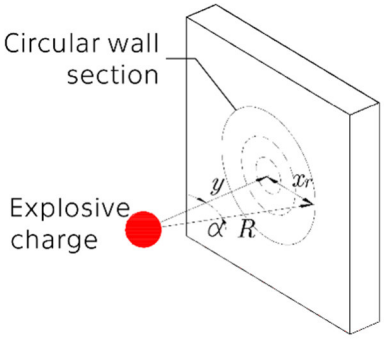

Figure 8: Close-in explosions - spatial arrangement

2.3.4 Confined Explosions

When a detonation of condensed explosives takes place within a confined space (inside a building or other structures), the pressures acting on a given confinement's surface (wall or slab) are amplified by their reflection from other surfaces. The reinforced blast wave pressures are known as shock pressures. In confined explosions, gas pressures, as described in Chapter 2.2.3, are also acting on the surrounding surfaces. The shock and gas pressures which escape through vent openings are referred to as leakage pressures - however, these are not within the scope of this thesis.

Due to reflections of the blast wave from different surfaces (in usually non-symmetric interior configurations) and their interactions with the primary wave, the time dependence of the loading, caused by shock pressures, is very complicated and difficult to define. In addition, this precise pressure-time history varies for each point within the structure. Therefore, the time dependence of shock pressures is set by employing a simplified triangular loading history. [4][11]

The distribution of loads on a single wall or slab is influenced by reflected waves, making it non-uniform, and challenging to define. In calculations, it is generally assumed that the load (both peak value and reflected impulse) is evenly distributed over the entire surface. This simplification is suitable for shear resistant surfaces. Properly reinforced concrete walls or slabs are usually

considered shear-resistant enough for this purpose. Shear resistance guarantees the transfer of localized loads to regions of lower stress.

The loading characteristics of a surface in a confined environment are, in practice, obtained from graphs (which can be found in UFC 3-340-02). These plots are constructed using the theoretical procedures based on semi-empirical blast data. The peak reflected blast pressures and reflected impulses depend on the effective charge weight, the size of the chamber, the position of the charge in the chamber and the configuration of the chamber - all with respect to the surface in question. [11]

If there is a need to calculate the magnitude of a blast load acting on only one part of a structure, a further simplification is required. To determine the load on a structural segment, the load parameters (both peak reflected pressure $P_{r\alpha}$ and reflected impulse $i_{r\alpha}$) of the air blast wave must be multiplied by a factor f_{sw} ranging between 1.5 and 1.75. This factor considers the secondary shocks. [4][11]

If the confinement is not fully vented (see Chapter 2.2.3), both gas and shock pressures will load the surrounding structures. To establish a loading history curve for a given surface, the maximum pressure value - either shock or gas - is used for each moment. [11]

2.3.5 Frangible Elements

If a structure (such as a wall or roof slab) or part of the confinement (such as a window or cover) fails during loading from a confined explosion, it impacts the interior gas and shock pressures, resulting in a decrease in their magnitude. Components that are intentionally designed to fail in these scenarios to safeguard the primary, frequently load-bearing structures, are known as 'frangible elements'. The effectiveness of interior pressure reductions is dependent on the area density of the frangible element and its ultimate resistance. Nonetheless, even elements that are extremely lightweight and weak can reflect some of the initial blast pressures before experiencing substantial deformation. However, they are effective in reducing gas pressures by providing additional venting area. Frangible elements are able to reduce the impulse of a confined explosion, although the peak reflected pressures remain unaffected.

If the resistance to outward motion is less than $1.2\ kN/m^2$, it is generally considered negligible. In such cases, the performance of a frangible element

depends solely on its area density. Graphs in UFC 3-340-02 can be used to easily evaluate the effects of these frangible elements for given boundary conditions. If the resistance is greater, its impact should be incorporated into the dynamic analysis of the issue.

For the reasons outlined in earlier paragraphs, it is advantageous to use light and weak or weakly supported covers as frangible elements. Suitable options may include gypsum boards or plexiglass boards supported by wooden frames. [11]

2.4 Response to Blast Loading

The calculations of structural responses to blast loading vary depending on the pressure design range. Typically, high, low, and very low-pressure ranges are examined, although the boundaries between them are indistinct. Nevertheless, certain semi-quantitative indicators of these boundaries will be presented. Figure 9 includes pressure/resistance-time graphs that illustrate different pressure design ranges.

In the high-pressure range, the peak reflected pressures exceed the resistance of the structure on which the load is applied. Nevertheless, the duration of the loading is over three times shorter than the time needed to reach the maximum deflection of the structure. In this range, reflected impulse becomes the vital load parameter for determining the structural response.

In the very low-pressure design range, maximum deflection is reached in the first tenth of the loading time. In this range, the structure's resistance can be compared to the peak reflected pressure.

The low-pressure design range falls between the previously stated ranges in terms of pressure magnitude and the ratio of load duration to the time taken for the structure to reach maximum deflection. Therefore, for this range, a dynamic analysis is necessary to obtain the structural response. [11]

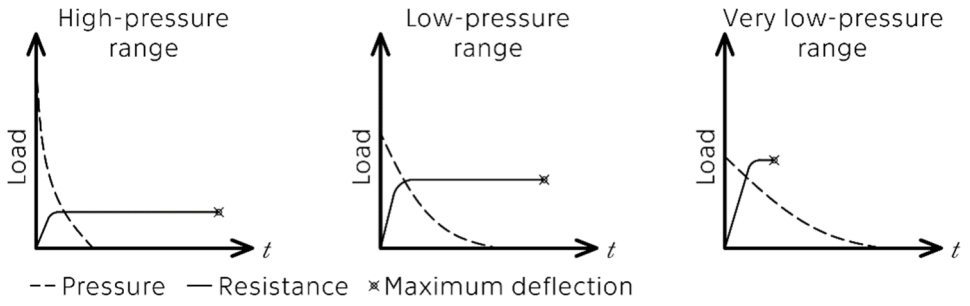

Figure 9: Design pressure ranges

2.4.1 High-Pressure Range

Due to the high reflected overpressures in the high-pressure range, the elastic component of the loaded structure's response is negligible. For reinforced concrete, a simplifying assumption of sufficient structural ductility to sustain large displacements under a constant load can be accepted.

Response calculations in the high-pressure range are typically split into two stages: loading and resistance. In the first phase, the velocity of a structure or segment is calculated based on the assumption that the structure provides no material or structural strength to resist the reflected impulse acting upon it. Only the inertia of the structure's mass is considered in this phase to resist the load. In the second phase, the structure's ultimate load carrying capacity resists the kinetic energy given to it in the first calculation phase. The output of this calculation is presented in the form of deflection δ or rotation θ of the structure. [20]

2.4.2 Low-Pressure Range

In the low-pressure design range, dynamic calculations are necessary to determine the response of the loaded structure. These calculations establish equilibrium between the sum of restoring forces S, damping forces F_D, inertia forces F_I, and the external loading forces F applied to the structure in a given direction (referred to as a degree of freedom). All of these forces exhibit a certain degree of time dependence. The forces on the left-hand side of the equation can be expressed as functions of displacement $u(t)$ and its derivatives. This leads to the following equation for a non-linear behaviour: [4][21]

$$\boldsymbol{M}\ddot{\boldsymbol{u}}(t) + \boldsymbol{C}\dot{\boldsymbol{u}}(t) + \boldsymbol{S}\big(\boldsymbol{u}(t)\big) = \boldsymbol{F}(t), \tag{2.7}$$

where $\boldsymbol{M}$ is the mass matrix, $\boldsymbol{C}$ is the damping matrix, $\boldsymbol{S}\big(\boldsymbol{u}(t)\big)$ is the vector of internal forces, $\boldsymbol{F}(t)$ is the vector of applied loads and $\boldsymbol{u}(t)$, $\dot{\boldsymbol{u}}(t)$, $\ddot{\boldsymbol{u}}(t)$ are the vectors of displacement, velocity, and acceleration, respectively. [21]

2.4.3 Damage Done to Concrete Structures

Concrete structures exposed to blast loading are generally assessed using criteria that rely on the physical appearance of the structure after it has been dynamically loaded. Diverse sources propose varying damage criteria, but they typically incorporate factors like the maximum rotation around the central axis

θ_{max} or the maximum achieved dynamic displacement δ_{max}. For reinforced structures, it is common to set the limits at $\theta_{max} < 5°$, where structural integrity must be maintained and $\theta_{max} < 10° - 12°$, where scabbing and significant plastic deformation are allowed. If δ_{max} exceeds the thickness of the structure, experiments have shown that scabbing (also known as secondary spallation – see Figure 10) and disintegration of concrete may occur. [20] [22]

Blast waves can also cause spalling of the loaded concrete wall or slab. When a blast wave reflects off a concrete structure, it creates a compression wave inside. The compression wave acts upon the structure's back face, resulting in tension waves being reflected into the structure from this surface. If the tension wave exceeds the dynamic tensile rupture strength of the material when interacting with the decaying compression wave, a portion of the back surface may separate. This early-time effect can generate high-velocity debris.[20] See Figure 10. Evaluation of spalling is above the scope of this thesis.

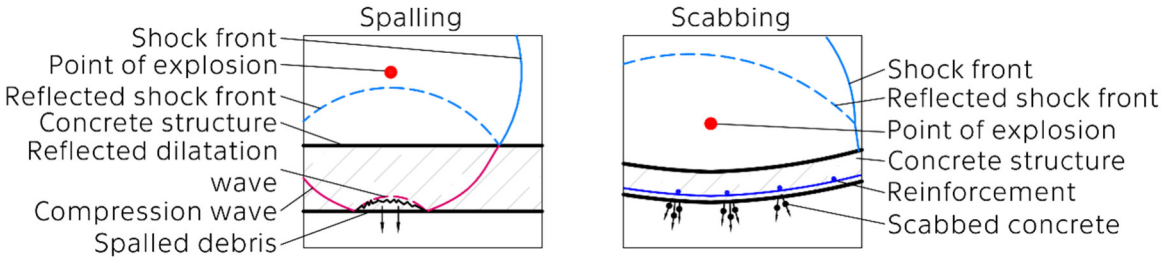

Figure 10: Spalling and scabbing

3 Goals

During the exploration of the subject matter, it was found that the method for response evaluation of reinforced concrete structures subjected to close-in explosions, described in NUREG/CR-0442, does not sufficiently express the plastic hinge radius of the damaged structure. This radius can be used as indicator of applicability of this method for structures with supports close to the 'epicentre' of the explosion on the loaded structure. It was also found that the method described in UFC 3-340-02 does not take into account the effect of fragmentation of frangible elements (which occur in case of e.g. glass covers) in its evaluation of blast loads caused by confined explosions. This publication also does not allow evaluation of impulse of gas pressures for partially vented confinements with multiple openings. It can be said that the application of mentioned methods on complex scenarios for response evaluation of concrete structures to confined explosions is not sufficiently done in available literature.

Based on these findings, the practical part of this thesis aims to apply and extend the methods outlined in NUREG/CR-0442 and UFC 3-340-02, enabling the evaluation of the structural response of a given structure subjected to a confined explosion in the case of a complex scenario (confinement with multiple openings, fragile frangible elements, etc.). Special focus is dedicated to the following areas:

- Obtaining the hinge radius of a wall segment deflected by a close-in explosion.
- Evaluating the reduction of reflection from the frangible element to the adjacent surface, caused by its fragmentation.
- Calculation of gas pressures in confined structures with multiple openings.
- Simple 'first-cut' evaluation of the structural response of reinforced concrete slab structures to confined blast loading.

4 Structural Analysis under Explosive Loading

This section of the thesis applies the theoretical concepts outlined in Chapter 2 to practical calculations. The chapter is divided into sections, each dedicated to specific comprehensive calculations. Firstly, it investigates the effects of a close-in explosion and the response of a concrete structure to it. Loading from confined explosions is the subject of the next sections. Chapter 4.3 examines the loading generated by the blast wave, while the Chapter 4.4 analyses loading produced by the gas pressures. Lastly, this paper presents an approach for calculating the response of concrete to blast loading. All the techniques presented in this thesis are applied to a single complex case study described in Chapter 4.1. The calculations executed are intended to evaluate consequences, not to design structures, and therefore, safety factors are not incorporated.

4.1 Case Study Setup

The aim of this case study is to demonstrate the calculation of loads generated by confined explosions and the subsequent response of concrete structures, all in the context of a real-world scenario. A room situated in a multistorey, monolithic concrete building serves as the explosion environment for this study. This analysis only considers the loadbearing and envelope structures.

The selected room has a rectangular prism shape. One side of the room (*W3*) features a large window (*O1*) and an undersill wall made of reinforced concrete. The other walls are also made of reinforced concrete. Wall *W4* has a large, uncovered entrance opening (*O2*). A spherical condensed charge of Octol 70/30 with a charge weight of $W_{EXP} = 6.3\ kg$ is placed inside this room. The detailed geometry of the case study setup is shown in Figure 11.

The concrete walls have thickness $d_w = 0{,}2\ m$ and are composed of C25/30 concrete, reinforced with B500B rebars (yield strength of the reinforcement $f_y = 500\ MPa$) that have a diameter of 10 mm. Both surfaces are evenly reinforced. The vertical and horizontal reinforcement have a spacing of 350 mm (cross-sectional area per unit width of bottom reinforcement is $a_{sy2} = 224\ mm^2/m'$ and top reinforcement is $a_{sy1} = 224\ mm^2/m'$ in both directions). This design fulfils the minimum requirements for wall reinforcement that are outlined in Eurocode

1992-1-1 and its Czech National Annex [23][24]. Transverse reinforcement is also present in the concrete walls. The schematics in Figure 12 demonstrate the reinforcement of concrete walls.

The characteristics of the floor slab structures are excluded as they are unnecessary for displaying the implementation of methods outlined in the succeeding chapters. The presumption is that the slab structures will be able to endure the blast loading. The double-glazed window in opening *O1* has dimensions of 4-16-4.

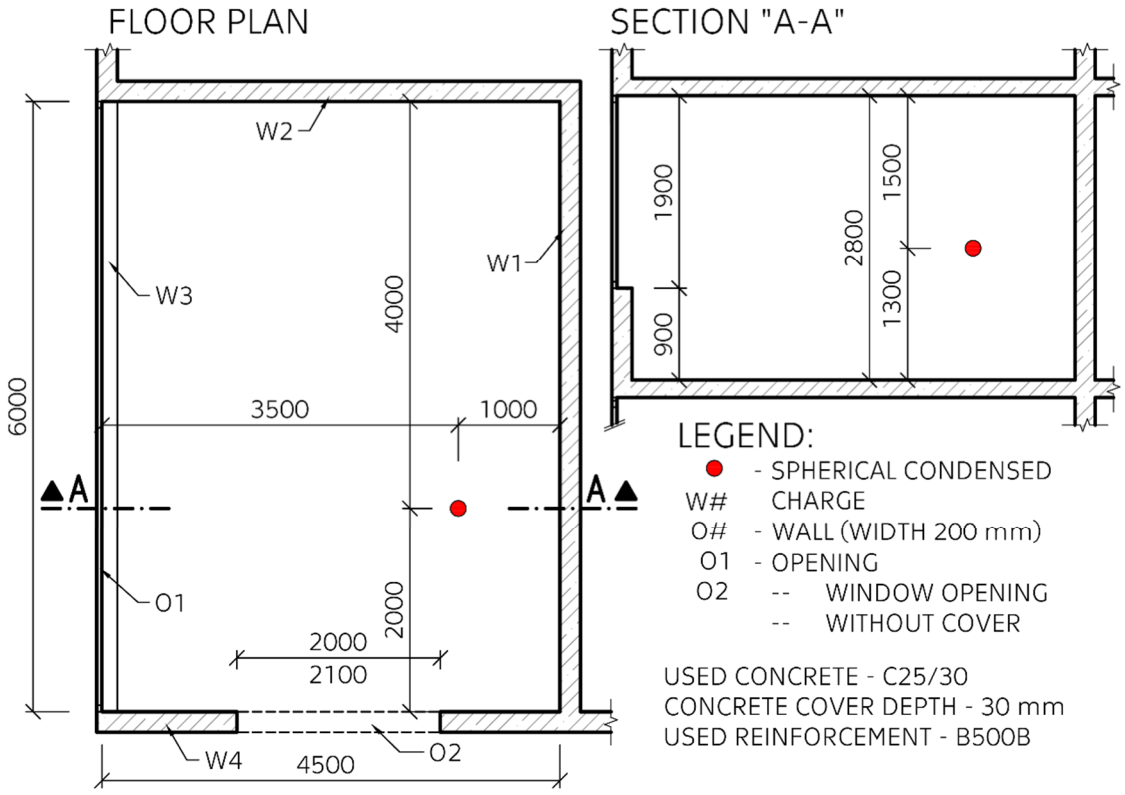

Figure 11: Case study - schematic layout drawing

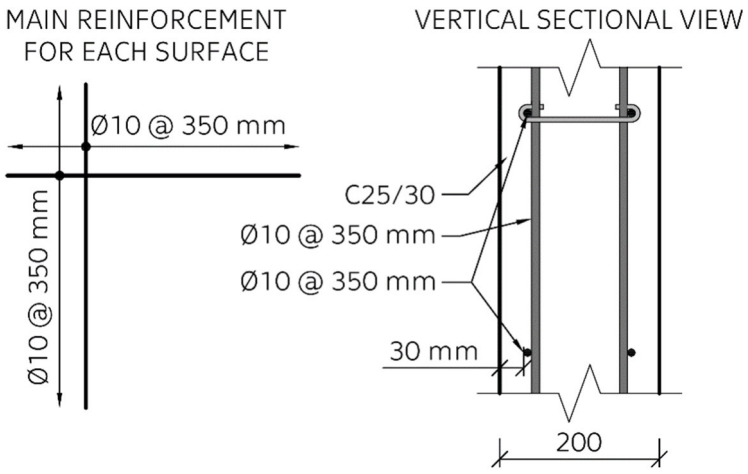

Figure 12: Case study - schematic drawing of reinforcement of concrete walls

4.2 Close-in Explosion

In this chapter, the calculation principles outlined in NUREG/CR-0442 are employed to calculate the response of reinforced concrete walls to close-in explosions. In Chapter 4.2.2, this thesis introduces a programmed method for calculating this problem, thereby enabling the determination of parameters that cannot be directly derived from the mentioned publication. The methodology implemented is based on the theoretical framework outlined in Chapter 2, especially in Chapter 2.3.3. The concrete structure's resistance and loading are expected to align with the high-pressure range as discussed in Chapter 2.4.1.

4.2.1 Procedure by NUREG/CR-0442

NUREG/CR-0442 provides graphs using scaled units from which the response of a given wall to a close-in explosion can be determined. These graphs are based on the following (notation of Figure 7 is used) [20]:

- The response of the concrete structure and the damage caused to it by the deformations will depend on the cylindrical wall segment bounded by a plastic hinge with a radius that corresponds to the maximum deformation value. This segment has a radius $x_{r,\delta max}$ (maximum deflection δ_{max}) or $x_{r,\theta max}$ (maximum rotation θ_{max}).
- Resisting forces F_R can be determined through simplified calculations based on the ultimate moment M_r of the reinforced concrete structure (the average of the ultimate moments calculated for the directions of the reinforcement):

$$F_R = 10\ M_r. \tag{4.1}$$

- The rotation angle θ is calculated from the deflection of the segment δ and the radius of the plastic hinge circle x_r, as shown in the following equation:

$$\theta = arctan(\delta / x_r). \tag{4.2}$$

- The deflection of the segment δ can be calculated using the equation below, which is based on the ratio of the kinetic energy (imparted to the segment by the blast wave's impulse) to the resisting forces F_R:

$$\delta = \frac{{i_T}^2}{2\ m_s F_r}, \tag{4.3}$$

where m_s is the mass of the segment and i_T is the total impulse acting on the segment, computed from the following equation:

$$i_T = \int_0^{x_r} i_{r\alpha}(x) \cdot 2\pi x\ dx\,. \tag{4.4}$$

- Reflected impulse, with consideration of the angle of incidence $i_{r\alpha}$, can be obtained from the graphs presented in Figures 4 and 6, as well as similar graphs from various sources that may exhibit slight variations (discussed later). For a given scaled distance Z is, from the air blast parameters graph, obtained the peak incident overpressure P_{so}. This overpressure is used along with the angle of incidence α to derive the peak reflected overpressure $P_{r\alpha}$ through the use of a $c_{r\alpha}$ to α graph. The air blast parameters graph is employed again, but this time, a fictitious scaled distance Z_{fic} is read for the value of peak normal reflected pressure P_r equal to the calculated $P_{r\alpha}$. The value of normal reflected impulse i_r subtracted from this graph for the fictitious scaled distance Z_{fic} is considered to be equal to $i_{r\alpha}$. It is important to consider, that certain quantities are in used graphs scaled by $W^{-1/3}$.

4.2.2 Programmed Calculation

The programmed calculation of close in explosion is based on calculating the deformation of the segment for various values of the radius x_r. The values of the radius $x_{r,i}$ used in this calculation satisfy the following conditions:

$$x_{r,i+1} = x_{r,i} + x_{r,step}, \tag{4.5}$$

$$\forall x_{r,i} \in \langle x_{r,step}; x_{r,lim} \rangle, \tag{4.6}$$

where $x_{r,step}$ and $x_{r,lim}$ alter the precision, scope, and complexity of the computation.

For a given radius $x_{r,i}$, the total impulse $i_{T,i}$ is determined initially. The integral presented in Eq. 4.4 is substituted with a sum of approximated total impulses $i_{T,n}$ acting on finite portions of the segment. The provided radius is separated into equal parts, dividing the plastic hinge circle into annuli with an equal width $x_{a,step}$, which is a user-selected value related to the calculation's accuracy. The reflected impulse $i_{T,n}$ acting on annulus n can be approximately determined as the result of multiplication of the area of the annulus $A_{a,n}$ and the reflected impulse $i_{r\alpha,n}$ for the radius of the intermediary axis of the annulus $x_{a,n}$. Geometric relations are shown in Figure 13. The entire calculation of the total impulse over the segment area is summarized in the following equation:

$$i_{T,i} \cong \sum_{n=1}^{x_{r,i}/x_{a,step}} A_{a,n} i_{r\alpha,n}(x_{a,n}) . \tag{4.7}$$

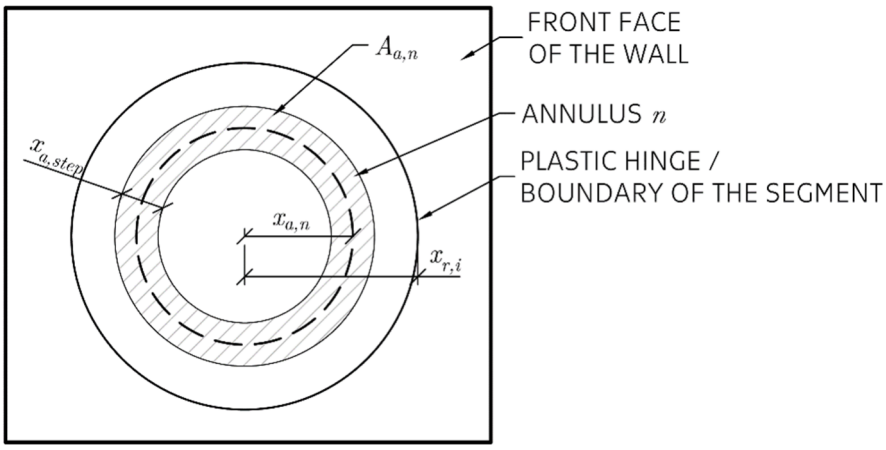

Figure 13: Approximate calculation of total impulse – geometric relations

Reflected impulse $i_{r\alpha,n}$ can be obtained in different ways – three methods were considered in this thesis. The first method involves determining it using the procedure outlined in NUREG/CR-0442 (as described in the last bullet point in 4.2.1) along with the graphs presented in NUREG/CR-0442 (Figure 14 a)). The second method is similar but employs UFC 3-340-02's graphs instead (Figure 14 b)). The third approach was to read the value of $i_{r\alpha,n}$ from graphs presented in UFC 3-340-02, which determines the dependence of reflected impulse on the angle of incidence [11] (Figure 14 c)). The values obtained from these methods were compared, and in general the results of different methods for the same inputs exhibited significant differences.

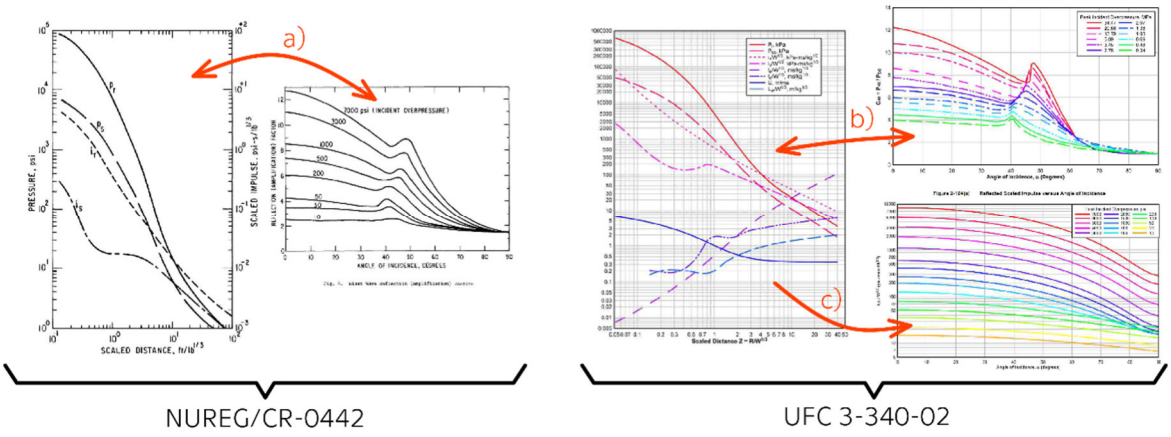

Figure 14: Approaches for obtaining $i_{r\alpha,n}$ [11][12][20]

For close in explosions, the NUREG/CR-0442 procedure and graphs are probably most suitable, because this approach leads to results that closely align with the results presented in NUREG/CR-0442. Additionally, these graphs consider the effect of pressure amplification at higher angles of incidence due

to reflection from the loaded wall. NUREG/CR-0442's $c_{r\alpha}$ to α graph, in comparison to the graph in Figure 6, has $c_{r90°} = 1{,}5$ [20].

Due to the numerous graph readings, $i_{r\alpha,n}$ should be obtained automatically through linear or logarithmic interpolation between the digitized points on the relevant graphs. The inputs for the readings can be derived from the geometric relations of the problem and use of Eq. 2.3. The derived equations utilize the notation from Figure 8:

$$Z_n = \frac{\sqrt{y^2 + {x_{a,n}}^2}}{\sqrt[3]{W}}, \tag{4.8}$$

$$\alpha_n = arctan\left(\frac{x_{a,n}}{y}\right). \tag{4.9}$$

After $i_{T,i}$ is computed for all examined radii $x_{r,i}$, the deformation is calculated for each radius using equations 4.2 and 4.3, where mass of the segment $m_{s,i}$ is calculated from following equation:

$$m_{s,i} = \rho_w d_w \cdot \pi \ {x_{r,i}}^2, \tag{4.10}$$

where ρ_w is the volumetric mass of the wall and d_w is its thickness.

The result of the programmed calculation includes the value of the maximal deflection δ_{max}, the radius of the plastic hinge circle corresponding to it $x_{r,\delta max}$, the maximal rotation θ_{max}, and once again, the radius of the plastic hinge circle relevant to this type of deformation $x_{r,\theta max}$.

4.2.3 Application

For the case presented in Chapter 4.1 , the approach described in the previous chapter is chosen for the calculation of the local response of wall *W1* (refer to Figure 11). This approach can be applied to this structure unless the radius of the plastic hinge corresponding to the maximal deformation is smaller than the distance between the 'epicentre' and the closest support of the wall (as assumed later in Eq. 4.12). While NUREG/CR-0442 specifies its method's applicability for charges with weights ranging from 23 kg to 9,000 kg [20], it can be reasonably assumed that, when dealing with structures thinner than those typically considered in the mentioned publication (which primarily focuses on nuclear power plant design), it is permissible to use smaller quantities of explosives and still obtain acceptable 'first-cut' results.

The primary blast wave is expected to cause the most severe loading of the wall before the reflected waves from other surfaces start to interfere with this wave, but the effect of these reflections on the local response can't be neglected. In the given scenario, it can be assumed that the peak reflected overpressure $P_{r\alpha}$ on the wall's most heavily loaded section will not increase due to secondary waves. However, the same cannot be stated for the total impulse i_T. The explosive's proximity to the loaded wall suggests that the increasing factor f_{sw} of the i_T will be lower than for other surfaces, but not negligible. Determining of the precise value of f_{sw} is not for the complexity of the problem easily possible.

Initially, it was necessary to calculate the equivalent charge weight W. The heat of detonation of TNT is $H^d_{TNT} = 6\ MJ/kg$ and of octol it is $H^d_{Octol} = 6.7\ MJ/kg$ [11]. The TNT equivalent is then[11]:

$$W = \frac{H^d_{Octol}}{H^d_{TNT}} W_{EXP} = \frac{6.7}{6} 6.3 = 7\ kg. \tag{4.11}$$

From the geometry of the setup (see Figure 11), other inputs for the calculation can be determined: the normal distance of the charge from wall *W1* $y = 1\ m$, and the value of the maximal plastic hinge radius assumption (as mentioned above) – as shown in the following expression:

$$x_{r,\delta max} \vee x_{r,\theta max} \leq 1.3\ m \quad \rightarrow \quad x_{r,lim} = 1.4\ m. \tag{4.12}$$

The upper limit of the calculated radius was chosen slightly larger to display the trend of results beyond the limit. The values of parameters associated with the precision of the calculation were chosen as follows: $x_{r,step} = 0.05\ m$ and $x_{a,step} = 0.01\ m$.

The volumetric mass of the reinforced concrete wall is assumed to be $\rho_w = 2\ 500\ kg/m^3$. The ultimate moment resistance for a given direction is calculated, with upper reinforcement neglected, as follows:

$$M_r = f_y a_{sy2}(d - 0.4x_c), \tag{4.13}$$

where the effective depth of the reinforcement is for horizontal direction $d_h = 165\ mm$, and for vertical $d_v = 155\ mm$. The concrete compression block depth x_c is calculated from the following equation:

$$x_c = \frac{f_y a_{sy2}}{0.8\ f_{cm}}, \tag{4.14}$$

where the mean compressive strength of concrete C25/30 is $f_{cm} = 33\ MPa$ [23]. After inputting the given values (some specified already in Chapter 4.1) into

equations 4.13 and 4.14 the outcomes are as follows: $x_c = 4.2\ mm$, $M_{r,h} = 18.29\ kNm/m'$ and $M_{r,v} = 17.17\ kNm/m'$. In the following calculations, the average ultimate moment $M_r = 17.73\ kNm/m'$ is taken into account.

Firstly, the specified inputs were used for the programmed calculation, as explained in Chapter 4.2.2, without taking into account the secondary waves ($f_{sw} = 1$). The results are presented below:

- Maximal displacement $\delta_{max} \geq 177\ mm$ reached in $x_{r,\delta max} = 1.4\ m$
- Maximal rotation $\theta_{max} = 7.9\ °$ reached in $x_{r,\theta max} = 1.05\ m$.

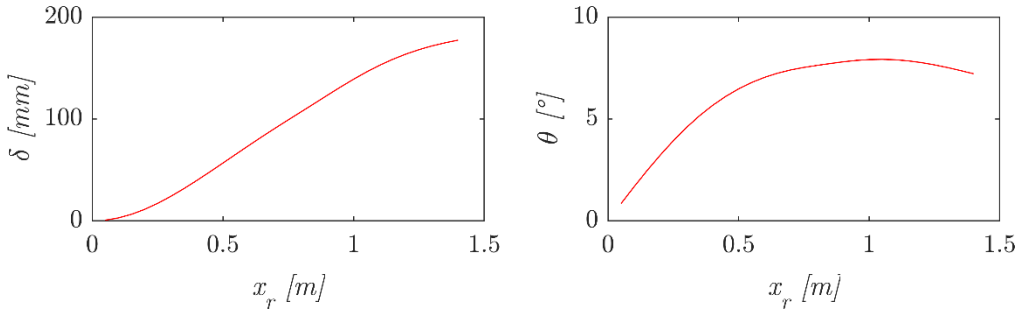

Figure 15: Close-in explosion results – deformation to segment's radius

For this input, no conclusions should be drawn from the calculated deflections δ, because its maximum value δ_{max} is not reached in the interval of x_r, where the local deflection is not influenced by supporting structures (see equation 4.12). On the other hand, the maximum rotation θ_{max} was reached in this interval. The result $\theta_{max} = 7.9\ °$ suggests that in the case where the reflected waves are neglected, the wall will undergo significant irreversible deformations and scabbing may occur after loading. However, it is unlikely that the structure will completely disintegrate at a local level.

Secondly, the calculation was repeated to account for the impact of reflected waves. Each $i_{T,i}$ was multiplied by varying factor of secondary shock waves $f_{sw} \in (1\ ; 1.75\rangle$. The calculation did not alter the x_r, where the maximum deformations occurred. It was found that a limiting value of $\theta_{max} = 12\ °$ was achieved with $f_{sw} = 1.24$. As outlined in Chapter 2.3.4, a lower limit of the multiplication factor is for simplified calculations set as $f_{sw,min} = 1.5$. From this result it can be deduced, that the section of wall *W1* closest to the charge is likely to disintegrate. However, for a more accurate assessment of the damage, more complex methods should be applied.

4.3 Blast Wave Loading from Confined Explosions

This chapter utilises UFC 3-340-02 as the basis for evaluation of blast loading resulting from confined explosions. UFC outlines a step-by-step procedure for obtaining the simplified loading history of a given surface. This procedure is summarised in chapter 4.3.1. This thesis extends this method to solve problems associated with the application of this method to more complex scenarios (in Chapter 0), such as the effects of fragmentation of the frangible elements. The approach is based on the theory presented in Chapter 2, particularly in chapters 2.3.4 and 2.3.5.

4.3.1 Procedure by UFC 3-340-02

UFC 3-340-02 outlines a method for obtaining simplified average loading parameters of a given surface, such as peak reflected overpressure $\overline{P_r}$ or reflected impulse $\overline{i_r}$. The procedure is summarised in this chapter. For the sake of clarity, the effect of adjacent frangible walls is explained in a separate section of this chapter. For its calculations, the UFC 3-340-02 uses various graphs, from which not all are presented in this work due to their quantity, but they can be obtained from the UFC – see source [11].

Evaluating Blast Loads [11]

A1) For a selected surface (the wall in question), determine the following parameters from the configuration of the surrounding structures: the number N of surfaces adjacent to the wall in question, the cross-sectional dimensions of the confinement structure H and L (if N is odd, H is the dimension between the free edge and the reflecting surface), the normal distances h and l of the charge to the nearest reflecting surfaces in the relevant directions, and the normal distance R between the charge and the wall in question.

A2) Calculate the inputs required for chart readings, including the ratios of h/H, l/L, L/H, L/R, and the normal scaled distance to the wall in question Z from Eq. 2.3.

A3) Read the values of $\overline{P_r}$ and $\overline{i_r}$ from the relevant UFC 3-340-02 graphs (example of those graphs is shown in Figure 23). In most cases interpolation between graphs will be necessary. Interpolations should be made in the logarithmic scale. If inputs fall outside the range of UFC 3-340-02's charts, logarithmic

extrapolation of the graphs is necessary for values that exceed Z or L/R. For values that exceed l/L or h/H, the limit value should be considered. If L/H values are greater than 5, they should be treated as equal to those corresponding to $L/H = 6$ read for the fictitious value of $L/R = 5H/R$.

Effect of Adjacent Frangible Walls [11]

B1) Carry out the procedure outlined in the previous section twice to evaluate the load on the wall in question: once with the frangible element in place and once without it. The resulting values are: $\overline{P_{r_{with'}}}$, $\overline{i_{r_{with'}}}$, and $\overline{i_{r_{without}}}$.

B2) To obtain the reflection factor f_r use a graph from Figure 16. Inputs for its reading are the area density of the frangible element $\rho_{A,f}$ scaled by $W^{-1/6}$ and the scaled distance Z, measured between the charge and the frangible element's surface.

B3) Average peak reflected pressure acting on the wall in question $\overline{P_r} = \overline{P_{r_{with}}}$. Calculate the average reflected impulse using the following equation:

$$\overline{i_r} = \overline{i_{r_{without}}} + (\overline{i_{r_{with}}} - \overline{i_{r_{without}}}) f_r. \tag{4.15}$$

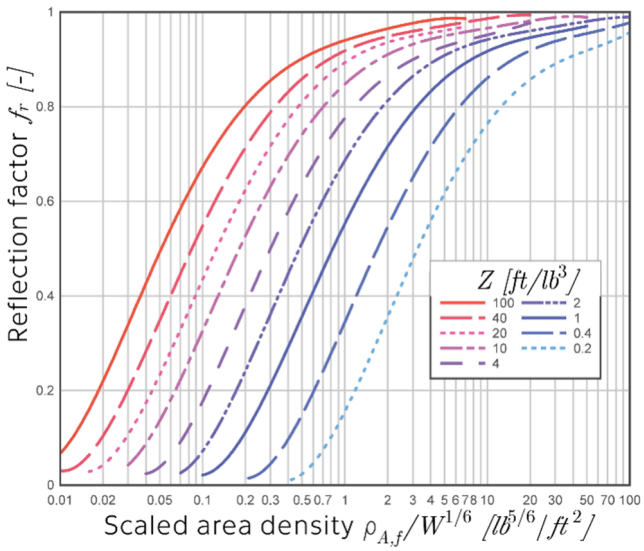

Figure 16: Reflection factor [11]

4.3.2 Expansion of the UFC 3-340-02 Method

The UFC 3-340-02 method is extended in this chapter, so it can be applicated to the case study in the subsequent chapter. This chapter is divided into three sections, each dedicated to a specific application problem.

Fragmentation of Frangible Elements

The UFC 3-340-02 states, that the effect of reflection from the frangible element to the adjacent surface should be reduced, when the frangible element breaks during loading, due to the creation of additional venting area [11]. This chapter evaluates this reduction.

In this method, the reflection factor f_r (from step B2)) is reduced by the average fragmentation coefficient $\overline{k_f} \in \langle 0\,;1\rangle$, so that Eq. 4.15 changes to the following form to take into account the effects of element 'break-up':

$$\overline{i_r} = \overline{i_r}_{without} + (\overline{i_r}_{with} - \overline{i_r}_{without}) f_r \overline{k_f}. \tag{4.16}$$

The average fragmentation coefficient $\overline{k_f}$ is dependent on the time evolution of the additional venting area A_{av}. This evolution should be examined only for the section of the frangible element between the wall in question and the charge (see Figure 17). This is due to the negligible reflection from the remaining part of the frangible element towards the wall in question (more on this in the following chapter on non-uniform surfaces). Area A_{av} can be calculated using the following equation:

$$A_{av}(u,t) = \max(A_f(u,t) - A_{f0} k_r(t)\,;0)\,, \tag{4.17}$$

where A_f denotes the area of the deformed surface of the relevant section (see Figure 18 a)), A_{f0} is the original area of the relevant section of the frangible element, k_r is the coefficient taking into account the rotation of the fragments, u is the displacement of the control point, and t is the time elapsed from the arrival of the primary shock wave to the control point. Equation 4.17 takes into account two phenomena that cause a reduction in the magnitude of the reflected wave. The first phenomenon is that the deformed shape of the frangible element has a larger area than its original shape (refer to Figure 18 a)), which must result in the creation of an additional venting area. The second phenomenon is taken into account by k_r – the rotation of the broken fragments of the frangible element can reduce the area of the fragment subjected to the load (see Figure 18 b)).

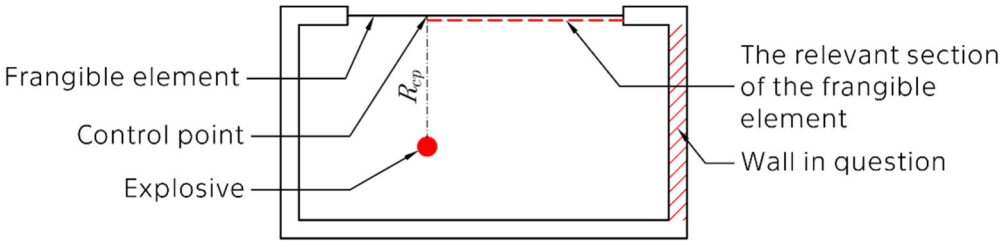

Figure 17: Spatial arrangement of the element section and control point

The contribution of rotation to the creation of the additional venting area is highly dependent on the size of the fragments. If the frangible element is expected to break into small pieces due to blast loading, then the effect of rotation is insignificant and can be neglected ($k_r = 1$). However, if rotation cannot be neglected, k_r should be obtained from the equation 4.18:

$$k_r(t) = \frac{A_{fp}(t)}{A_{f0}}, \tag{4.18}$$

where A_{fp} is the area of all fragments projected onto the plane orthogonal to the propagation of the blast wave in a given time t. This area should be probably obtained by statistical methods due to the complexity of the movement of the fragments. Further specification of this problem is above the scope of this thesis.

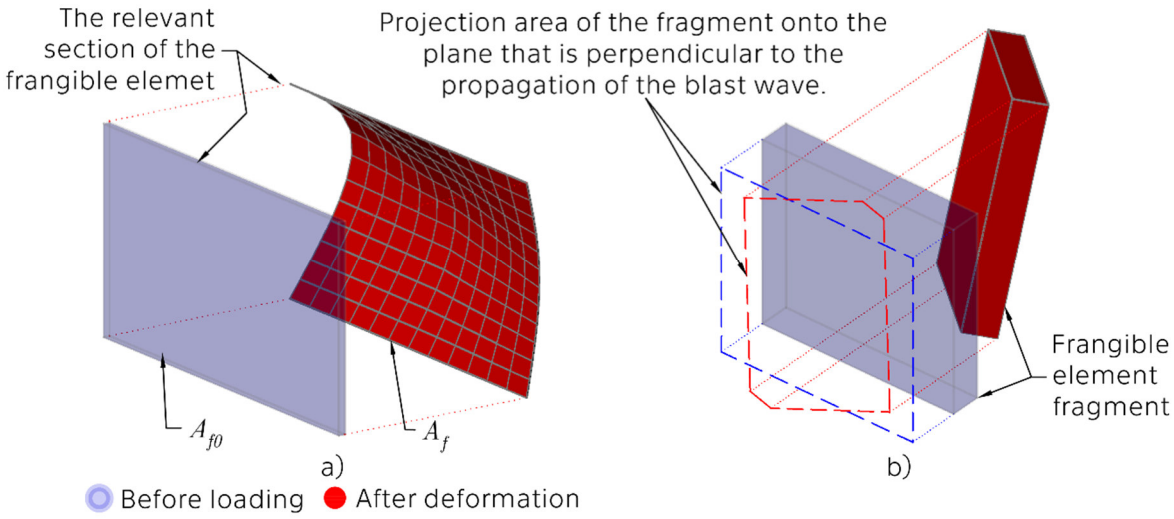

Figure 18: Formation of additional venting area due to fragmentation

The evaluation method for $\overline{k_f}$ assumes, that the primary reflections constitute the predominant source of pressure amplification on the wall in question. Therefore, the waves that reflect from multiple surfaces can be neglected. Additionally, it is assumed that the frangible element has little resistance to blast loading (see Chapter 2.3.5), and the time to failure (fragmentation) is assumed to be zero.

Before performing the calculations, it is necessary to define the simplified shape of the deformed frangible element on which the calculation of $A_f(u,t)$ depends. It is assumed that this shape will emulate the front of the primary blast wave. A number of the most common simplified shapes are shown in Figure 19. The ideal representative simplified shape for a specific scenario depends on the arrangement of the confinement structure and the explosive.

The simplified shape shown in Figure 19 a) should be used when the explosion occurs close to the frangible element and the reflected waves have a negligible influence on the shape of the primary blast wave front. Shape from Figure 19 b) is appropriate when reflections from two opposite sides cannot be ignored. Ultimately, Figure 19 c) demonstrates a deformed shape that is fitting for configurations where the reflections from all surfaces surrounding the frangible element have a significant influence on the shape of the blast wave front.

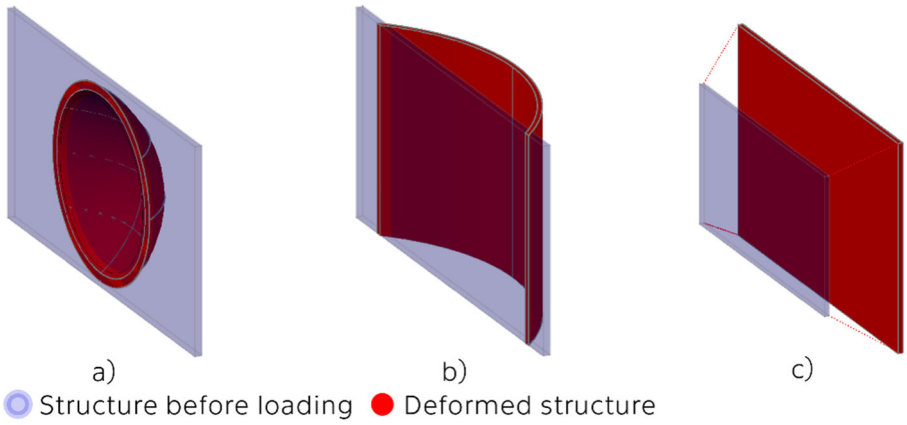

Figure 19: Simplified shapes of deformed frangible element

Each deformed surface can be defined by the deflection u of the control point - the perpendicular projection of the point of explosion onto the plane of the frangible element - and a second parameter. In shape a), this parameter is the diameter of the cap base, while for shape b), it is the chord length. Both mentioned parameters can be measured between the points where the blast wave front intersects the plane of the frangible element. For shape c), the second parameter is the angle that determines the expansion of the fragmented frangible element. If the simplified shape exceeds the frangible element in its plane (for either a) or b) from Figure 19), it is necessary to define the edges of this deformed shape for the calculation of A_f.

The fragmentation coefficient k_f for a given time t and deflection of the control point u can be calculated with use the following equation:

$$k_f(u,t) = \max\left[\left(1 - \frac{A_{av}(u,t)}{A_{f0}}\right)^2; 0\right]. \tag{4.19}$$

Equation 4.19 is based on the following conditions. Firstly, the condition $A_{av} = 0 \rightarrow k_f = 1$ must be satisfied. Secondly, if $A_{av} \geq A_{f0}$, then the reflection of the wave towards the interior is negligible. This assumption is based on the

principle of the wave leaking around the fragments, which is discussed in Chapter 2.3.1. However, reflections can be neglected only if the clearing time t_c, which depends on the size of the fragments, is less than the time taken to reach the deformation of the frangible element $A_{av} = A_{f0}$. In other words, this method is suitable for fragment sizes where $A_{av}(u(t_c), t_c) \leq A_{f0}$. Additionally, it is suggested that the reduction in reflection is more pronounced with a difference of smaller values of A_{av}, than with the same difference of larger values of A_{av}. This belief is based on the fact that the pressure gradient in the gaps is increased when the fragments are close to each other. Therefore, the drop of reflected overpressures (clearing) in front of the fragments should be increased. Equation 4.19 accounts for this phenomenon by squaring the expression. However, to obtain more accurate results, this engineering estimate should be refined by experiment or numerical simulation.

The average fragmentation coefficient $\overline{k_f}$ can be acquired via time-stepping calculation as a weighted average of $k_{f,i-1/2}$ – the approximate average fragmentation coefficient of time step i. The weights are the reflected impulses that act on the control point during the given time step. The calculation typically has the following initial conditions:

$$u(t = 0) = 0, \tag{4.20}$$

$$\dot{u}(t = 0) = 0, \tag{4.21}$$

$$k_f(t = 0) = 1, \tag{4.22}$$

where $u(t)$ is the displacement of the control point of the deformed frangible element, $\dot{u}(t)$ is its first derivative (velocity). Its second derivative $\ddot{u}$ (acceleration) is for a given time t, calculated from the following equation derived from the second law of motion:

$$\ddot{u}(t) = \frac{P_{cp}(t)}{\rho_{A,f}}, \tag{4.23}$$

where $\rho_{A,f}$ denotes the area density of the frangible element and P_{cp} is the pressure acting on the fragments at the control point.

This pressure and its time dependence rely on the chosen simplified shape of the deformed frangible element, as well as the size of the fragments. Because the fragments move in the direction of the propagating blast wave, drag pressures weaken and can usually be neglected. If the drag pressures are not taken into account and the fragments are small enough for $A_{av}(u(t_c), t_c) \leq A_{f0}$ to

hold, then the pressures acting on the fragments at the control point $P_{cp}(t)$ for the simplified shapes a) or b) can be extracted from the simplified triangular history of reflected pressures, which are influenced by the fragmentation. The history of P_{cp} should take into account the effect of secondary waves by employing f_{sw}. Please refer to the following expression:

$$P_{cp}(t) = max\left[P_{r,cp}\left(1-\frac{t}{t_{r,cp}}\right) f_{sw} k_f(t); 0\right], \tag{4.24}$$

where $P_{r,cp}$ is the peak normal reflected overpressure in the control point and $t_{r,cp}$ denotes the fictitious duration of positive loading duration in the control point. The latter can be calculated using the following equation:

$$t_{r,cp} = \frac{2\ i_{r,cp}}{P_{r,cp}}, \tag{4.25}$$

where $P_{r,cp}$ is the peak normal reflected overpressure in the control point and $i_{r,cp}$ is the normal impulse of the reflected pressures in the control point.

The quantities that characterize the time step i can be derived from the previous time step $i-1$ and the loading history of fragments in the control point. The calculation utilises the Eq. 4.26 derived for this application (for notation see Figure 20). This equation matches the linear acceleration method [25]:

$$u_i = u_{i-1} + \dot{u}_{i-1} t_{step} + \frac{1}{6}(2\ \ddot{u}_{i-1} + \ \ddot{u}_i){t_{step}}^2, \tag{4.26}$$

where $\ddot{u}_i = \ddot{u}(t_i)$ and can be obtained from Eq. 4.23. Since $\ddot{u}_i$ varies with $P_{cp,i}$ and $P_{cp,i}$ always depends on $k_{f,i}$, which in turn depends on $A_f(u_i, t_i)$ (refer to equations 4.17 and 4.19), it can be concluded that $\ddot{u}_i$ is dependent on u_i. Therefore, an iterative calculation is required. Firstly, the value of $k_{f,i}$ is estimated as $k_{f,i} = k_{f,i-1}$. Then, the calculation is performed using equations 4.23 and 4.26 resulting in an approximate value of u_i. This value is then used for a better guess of $k_{f,i}$ (calculated from the equations 4.17 and 4.19). This cycle continues until the difference of u_i between subsequent iterations is under the limiting value u_{lim}. This value modifies the accuracy of the calculation.

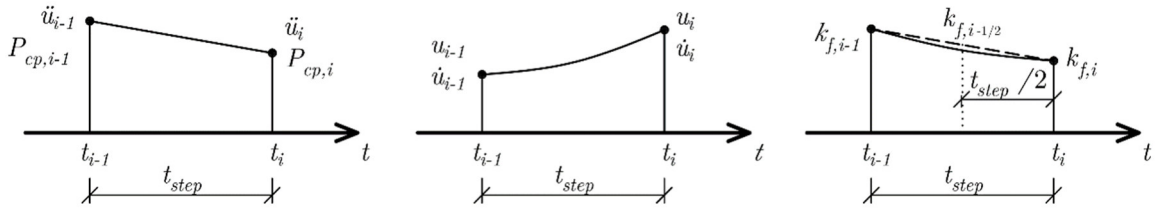

Figure 20: Scheme of quantities used in time-stepping calculation

The velocity at the end of the time step $\dot{u}_i$ can be obtained from the following equation:

$$\dot{u}_i = \dot{u}_{i-1} + \frac{1}{2}(\ddot{u}_{i-1} + \ddot{u}_i)t_{step}. \tag{4.27}$$

The approximated average fragmentation coefficient of the time step i is then obtained as:

$$k_{f,i-1/2} = \frac{k_{f,i-1} + k_{f,i}}{2}. \tag{4.28}$$

And finally, the average fragmentation coefficient $\overline{k_f}$ is calculated, for $t_{step} = const.$ as follows:

$$\overline{k_f} = \frac{\sum_{i=1}^{t_{r,cp}/t_{step}} k_{f,i-1/2} \frac{P_{cp,i-1} + P_{cp,i}}{2}}{\sum_{i=1}^{t_{r,cp}/t_{step}} \frac{P_{cp,i-1} + P_{cp,i}}{2}}. \tag{4.29}$$

Reflection From Non-uniform Surfaces

The effect of blast wave reflection from non-uniform surfaces to the wall in question is not specified in UFC 3-340-02. This chapter proposes a simplified approach to this problem.

Based on the procedure presented in Chapter 4.3.1 it can be concluded that the confinement structures that do not stand in the space defined by the explosion point and the wall in question have little or no effect on the pressures acting on the wall in question. As a result, the areas of surfaces that are "behind" the charge should not be considered.

Reflection from non-uniform surfaces "in front" of the explosive can be evaluated by the reflection factor f_r, which is calculated as a weighted average of the reflection factors $f_{r,n}$ (if necessary, taking into account the fragmentation $f_{r,n}\overline{k_f}_n$) of individual uniform sections n of the surface. The reflected factor of an uncovered opening is $f_{r,n} = 0$ and for a solid non-frangible surface, it is $f_{r,n} = 1$. Weights for this type of calculations can be determined using the surface area of the section $A_{s,n}$, or the solid angle $\Omega_{s,n}$ measured from the point of explosion. Another option for obtaining weights is by combining angle and distance – the angle that the section occupies $\alpha_{s,n}$ in one plane and the section height $h_{s,n}$ in the orthogonal plane. The choice depends on the shape of the primary shock wave that comes into contact with the non-uniform surface. The shape of the front is determined by the arrangement of the explosive, confinement, and the

non-uniform section. The heights of the triple points can be used to visualize the shape of the front.

An illustrative example is depicted in Figure 21 - the wall in question is shown in red. In this example, to calculate f_r it is advisable to neglect opening 1 because it is "behind" the charge. However, the openings 2 and 3 are located "in front" of the charge, so they should be taken into account. For opening 2, the suitable weights would be the solid angles, since the front of the blast wave is expected to be spherical, due to its proximity to the explosive. For opening 3 the most appropriate weights would be the horizontal angle $\alpha_{s,3}$ and the vertical height $h_{s,3}$, as the wave is expected to be vertically nearly flat due to floor and ceiling reflections. If the surface area would be used as the weight for $f_{r,3}$, the result is unlikely to be significantly different. This is because the wall with opening 3 is too short when compared to the normal distance of the charge from this wall, making the difference insignificant.

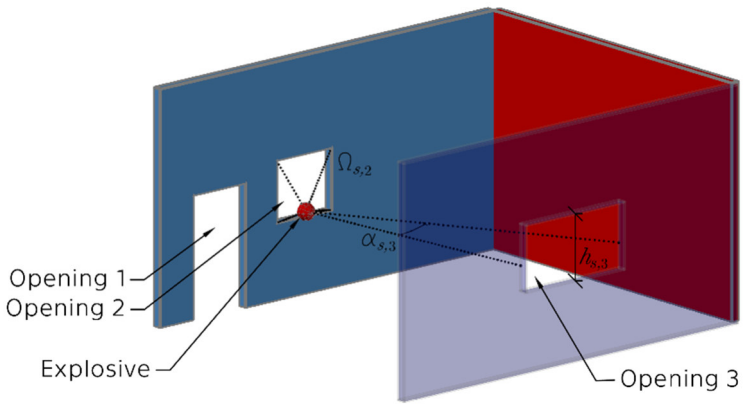

Figure 21: Non-uniform surfaces – an example of spatial arrangement

L/H Lower Limit

If inputs fall outside the chart range used for calculations of $\overline{P_r}$ and $\overline{i_r}$ UFC 3-340-02 specifies an approach to obtain the required values - see step A3) from Chapter 4.3.1. However, the procedure for deriving $\overline{P_r}$ and $\overline{i_r}$ for values $L/H < 0.625$ is not defined by UFC 3-340-02. From the graphical charts, it is evident that $\overline{P_r}$ and $\overline{i_r}$ values always decrease with decreasing values of $L/H \leq 1.25$. Therefore, it is safe to utilise the limiting values (values of $\overline{P_r}$ and $\overline{i_r}$ read for $L/H = 0.625$) for subsequent calculations.

4.3.3 Application

For the case outlined in Chapter 4.1, the method from Chapters 4.3.1 and 0 is chosen to calculate the blast load acting on the wall *W2* (see Figure 11).

Initially, the loading parameters of the wall *W2* were carried out for the case where the frangible element acts as a rigid wall. The geometric inputs for this scenario are displayed in Figure 22 a). Subsequently, the inputs for chart readings are as follows: $N = 4$, $h/H = 0.46$, $l/L = 0.22$, $L/H = 1.61$, $L/R = 1.12$, and $Z = 2.09\ m/kg^{1/3}$. The adequate UFC 3-340-02 graphs were examined using the AutoCAD software to obtain the reading – see Figure 23 a) and b). Since the value of the scaled distance Z exceeds the limit provided by the graphs $Z_{lim} = 1.59\ m/kg^{1/3}$, the values of $\overline{P_r}$ and $\overline{i_r}$ were logarithmically extrapolated from the readings for the values of Z_{lim} and $Z_2 = 0.79\ m/kg^{1/3}$. The results of this section have been derived through logarithmic interpolation of the read values. They are as follows: $\overline{P_{r_{with}}} = 456\ kPa$ and $\overline{i_{r_{with}}} = 1400\ kPa \cdot ms$ (taking into consideration the scaling of $\overline{i_r}$ values in the graphs by $W^{-1/3}$).

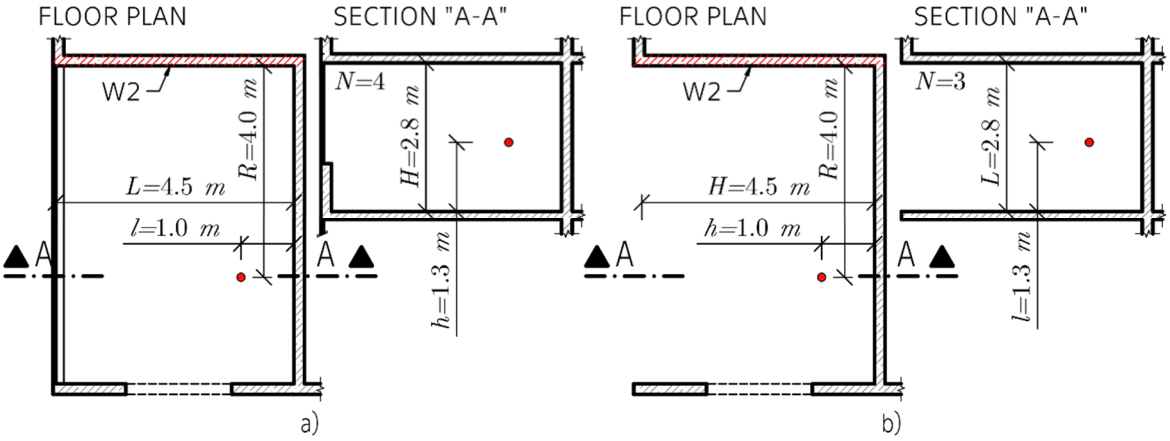

Figure 22: Geometric inputs to confined explosion calculation

The same procedure was carried out for the case without wall *W3*. The geometric inputs for this scenario are shown in Figure 22 b). The chart readings inputs are then as follows: $N = 3$, $h/H = 0.22$, $l/L = 0.46$, $L/H = 0.62$, $L/R = 0.7$, and $Z = 2.09\ m/kg^{1/3}$. The same procedure as previously described was followed with the exception that the values for L/R and L/H are in this case smaller than the limit provided by the graphs $L/R_{lim} = 1$ and $L/H_{lim} = 0.625$. The extrapolations for L/R were made graphically using AutoCAD software – see Figure 23 c). The values of $\overline{i_r}$ were read for the limit values L/H_{lim} as advised in the last section of Chapter 0. The result of this part of the calculation is $\overline{i_{r_{without}}} = 1190\ kPa \cdot ms$. (taking into consideration the scaling of $\overline{i_r}$ values in the graphs by $W^{-1/3}$).

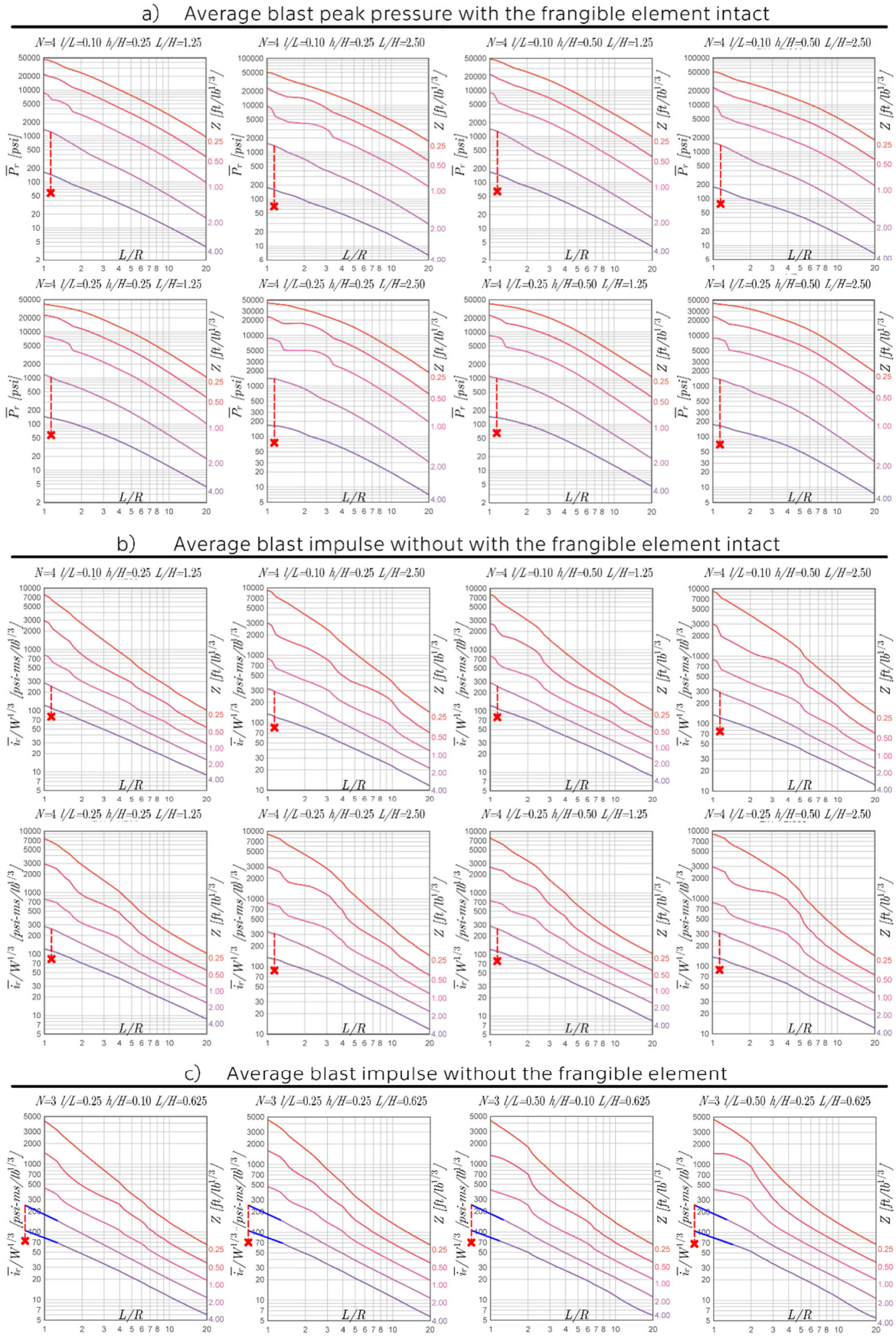

Figure 23: Confined explosion: blast pressure / impulse graphs readings [11]

The reflection factor $f_{r,O1}$ of the window (*O1*) was determined using the graph from Figure 16. The glass volumetric mass was assumed to be $\rho_{fr} = 2500\ kg/m^3$. The width of the frangible element was taken as the sum of widths of the two glass sheets $d_{fr} = 8\ mm$. This leads to the area density of the window to be $\rho_{A,f} = 20\ kg/m^2$. The window is located at a distance of $R = 3.5\ m$ from the explosion point. Thus, the inputs for the graph reading are as follows: $Z = 1.83\ m/kg^{1/3}$ and $\rho_{A,f}/W^{1/6} = 14.46\ kg^{5/6}/m^2$. The reading is $f_{r,O1} = 0.89$.

The average fragmentation coefficient $\overline{k_f}$ was determined using programmed iterative calculation. The simplified shape b) from Figure 19 was chosen as the shape of the deformed frangible element, since the front of the blast wave has an almost flat profile in the vertical direction - see Figure 24 (the heights of the triple points were calculated according to Eq. 2.6). Consequently, the area of the section's deformed surface $A_f(u,t)$ can be computed using the following equation:

$$A_f(u,t) = A_{f0} - h_{fr}x_{real}(t) + h_{fr}R_{fikt}(u,t)\,\mathrm{atan}\frac{x_{real}(t)}{R_{fikt}(u,t) - u}, \tag{4.30}$$

where h_{fr} is the height of the frangible element (in this case $h_{fr} = 1.9\ m$), $x_{real}(t)$, $R_{fikt}(u,t)$, and A_{f0} are calculated according to the following equations:

$$x_{real}(t) = \min(x_{fr}(t); x_{\lim}), \tag{4.31}$$

$$R_{fikt}(u,t) = \frac{u^2 + {x_{fr}}^2}{2u}, \tag{4.32}$$

$$A_{f0} = x_{\lim}h_{fr} = 7.6\ m^2, \tag{4.33}$$

where $x_{\lim}$ corresponds to the length of the section (in this case $x_{\lim} = 4\ m$), and x_{fr} represents the distance between the control point and the intersection of the blast wave's front and the plane of the frangible element (without considering its distortion by the frangible element). This distance can be obtained from the following equation:

$$x_{fr}(t) = \sqrt{R_{wf}(t)^2 + {R_{cp}}^2}, \tag{4.34}$$

where R_{cp} represents the distance between the explosive and the control point, and R_{wf} denotes the radius of the wavefront. This value can be acquired from the graph presented in Figure 4, where the value of Z can be read for a given $t_A = t + t_{A,cp}$. Equations 4.30 to 4.34 are derived from the geometry of the problem depicted in Figure 25.

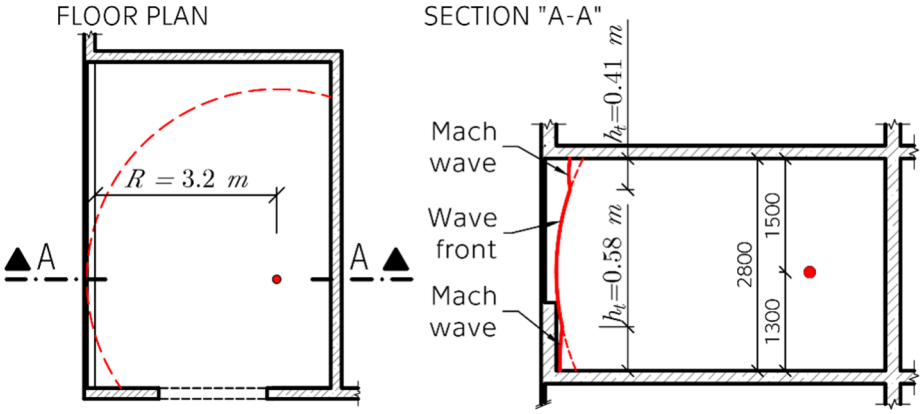

Figure 24: Wavefront shape prior to its collision with wall W3

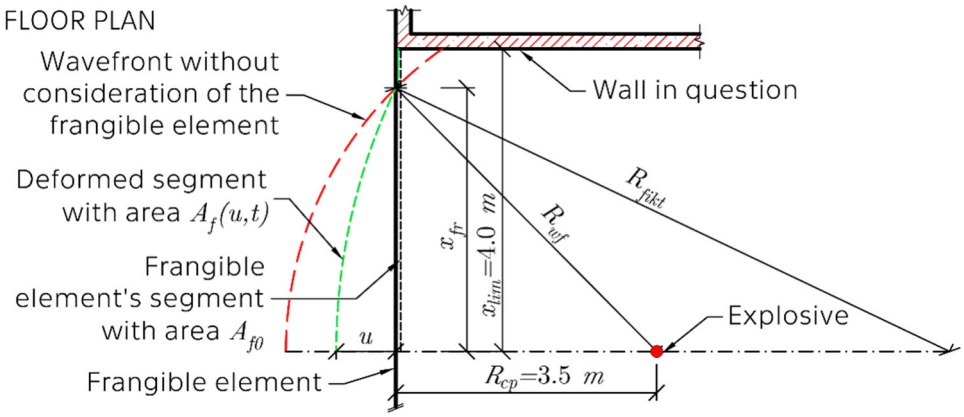

Figure 25: Geometry of the frangible element's deformed shape

The glass fragments are anticipated to be small; therefore, it is reasonable to assume that $k_r = 1$. Additionally, the condition $A_{av}(u(t_c), t_c) \leq A_{f0}$ is expected to be satisfied. Consequently, Equation 4.24 can be employed for calculating P_{cp} for a given time t. The estimated effect of reflected waves on the load of the control point is represented by coefficient $f_{sw} = 1.75$. In establishing the initial conditions, the parameters outlined in Equations 4.20, 4.21, and 4.22 were employed. The initial acceleration was determined using Eq. 4.23 and 4.24 with $t = 0$ and $P_{r,cp} = 1\ 460\ kPa$, as obtained from Figure 4 for $Z = R_{cp}/W^{1/3} = 1.83\ \ m/kg^{1/3}$. Thus $\ddot{u}(t = 0) = 0.073\ m/ms^2$.

The process of acquiring the average fragmentation coefficient was carried out iteratively, as described in Chapter 0, using MATLAB software. The time-step was set to $t_{step} = 43.2\ \mu s$ and the iteration threshold to $u_{\lim} = 10\ \mu m$. Figure 26 illustrates the evolution of selected quantities over time. The result of this calculation is $\overline{k_f} = 0.99996 \cong 1$, indicating that the impact of the additional venting area caused by window fragmentation can be disregarded in this instance.

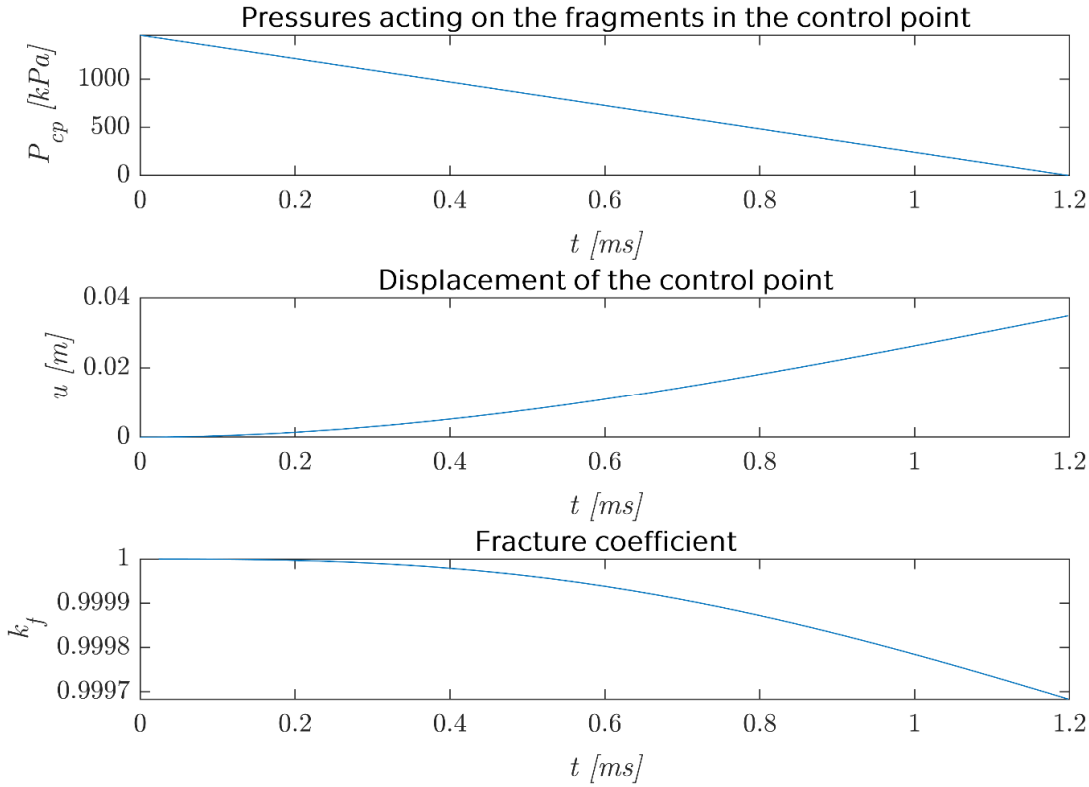

Figure 26: Calculation of $\overline{k_f}$ - time evolution of selected quantities

The reflection factor f_r of wall *W3* was then calculated as a weighted average of the reflection factors of individual uniform surfaces, namely the undersill (with height $h_{undersill} = 900\ mm$ and reflection factor $f_{r,undersill} = 1$) and the window. The weights were determined based on the heights of each surface. The reason for this is that the blast front in the vertical direction, in front of the wall is almost flat (as shown in Figure 24), and in the horizontal direction both surfaces extend over the entire wall. As a result, the reflection factor was calculated as follows:

$$f_r = \frac{f_{r,O1}\ \overline{k_f} h_{fr} + f_{r,undersill} h_{undersill}}{h_{fr} + h_{undersill}} = 0.93. \tag{4.35}$$

Finally, it was possible to determine the average loading parameters acting on the wall *W2*. The average peak reflected overpressure is $\overline{P_r} = \overline{P_{r_{with}}} = 456\ kPa$ and the average reflected impulse is calculated to be $\overline{i_r} = 1\ 388\ kPa \cdot ms$ using Eq. 4.15. The fictitious duration of the triangular loading history can be calculated from the following equation:

$$\overline{t_r} = \frac{2\ \overline{i_r}}{\overline{P_r}} = 6.1\ ms. \tag{4.36}$$

4.4 Gas Pressures

This chapter describes a systematic process for acquiring a simplified loading history of confinement surfaces. It utilises UFC 3-340-02 as the basis for calculating gas loading. This part of the thesis also extends the UFC method, so it can deal with scenarios where there are multiple openings in the structure (in Chapter 4.4.2). The approach follows the principles presented in Chapter 2, in particular in sections 2.2.3 and 2.3.5.

4.4.1 Procedure by UFC 3-340-02

This chapter summarises two procedures defined by UFC 3-340-02. One is for the evaluation of gas pressures and the other is for the evaluation of shock loads acting on frangible elements (both are used later in Chapter 4.4.3).

Evaluating Gas Pressures [11]

C1) Determine the peak gas pressure P_g from graph shown in Figure 27, for the value of equivalent charge weight to free volume ratio W_g/V_f.

C2) Determine the inputs for further calculations – total venting area scaled by the free volume ${A_v/V_f}^{2/3}$, scaled area density of the frangible cover of the opening ${\rho_{A,f}/W_g}^{1/3}$, and the scaled average reflected impulse acting on the structure containing the vent opening ${\overline{i_r}/W_g}^{1/3}$ – in a case of an opening with frangible cover use procedure outlined in following section, otherwise use the method presented in Chapter 4.3.1.

C3) Determine the gas impulse i_g from the relevant ${i_g/W_g}^{1/3}$ to ${A_v/V_f}^{2/3}$ UFC 3-340-02 graphs (example of those graphs is shown in Figure 28), for inputs from the previous step. In most cases logarithmic interpolation between graphs will be necessary. Determine the duration of gas pressures with use of Eq. 2.4.

Evaluating Average Shock Loads on Frangible elements [11]

D1) Determine the loading parameters $\overline{P_r}$ and $\overline{i_r}$ acting on the frangible element, as outlined in Chapter 4.3.1, assuming that it will remain intact.

D2) Evaluate the reflection factor f_r, with use of graph shown in Figure 16, for scaled area density $\rho_{A,f}/W^{1/6}$ and the fictitious scaled distance Z_{fic} read from the graph in Figure 4 corresponding to reflected impulse $i_r = \overline{i_r}$.

D3) The average peak reflected pressure acting on the frangible element is $\overline{P_{r\,fr}} = \overline{P_r}$ and the average impulse contributing to the translation of the frangible element is $\overline{i_{r\,fr}} = f_r \overline{i_r}$.

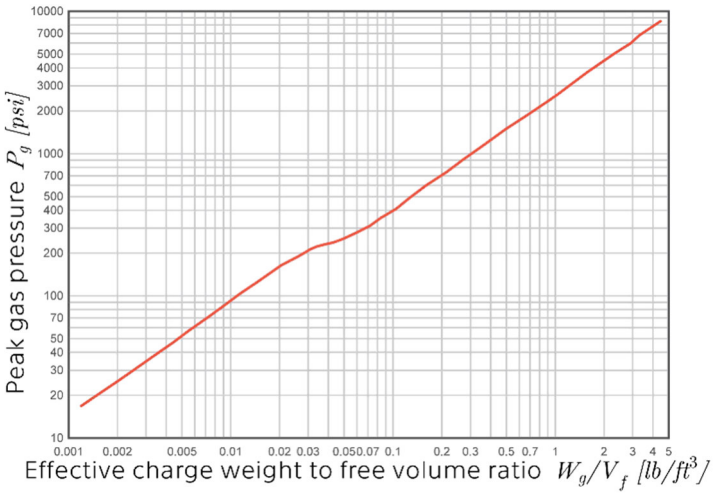

Figure 27: Peak gas pressures [11]

4.4.2 Considering Multiple Openings

The UFC 3-340-02 method does not specify the approach for scenarios where there are multiple openings in the confinement structure. As the procedure determines i_g directly from graphs, assessing the impact of multiple openings is not simple. This chapter discuss a method of using the UFC 3-340-02 graphs to assess gas pressures in these circumstances.

At first, the procedure outlined in Chapter 4.4.1 must be executed individually for each opening, without accounting for the others. Each variable, distinct for every opening, is indexed with the identification number i of the respective opening. Subsequently, the fictitious scaled vent areas, denoted as $A_{v,i,fic}/V_f^{2/3}$ are read for calculated gas impulses $i_{g,i}$ from a $i_g/W_g^{1/3}$ to $A_v/V_f^{2/3}$ graph. The resulting actual gas pressure i_g, considering multiple openings, is then extracted from the same graph for the sum of the fictitious scaled areas.

For this approach, it is necessary to define parameters W_g/V_f, $\overline{i_r}/W_g^{1/3}$, and $\rho_{A,f}/W_g^{1/3}$, which characterize the shape of the $i_g/W_g^{1/3}$ to $A_v/V_f^{2/3}$ graph used for the procedure described in previous paragraph. For the first mentioned parameter the actual value of W_g/V_f should be considered. However, the same approach cannot be employed for the parameter $\overline{i_r}/W_g^{1/3}$, due to its variations between openings. To ensure the accuracy, the value of $\overline{i_r}/W_g^{1/3}$ should ideally

fall within the range of values used for the individual openings - $\overline{i_{r_i}}/{W_g}^{1/3}$. Openings with a more substantial impact on the drop of gas pressures should exert greater influence on the parameter $\overline{i_r}/{W_g}^{1/3}$. In this thesis, this is achieved by calculating this parameter as a logarithmic weighted average of $\overline{i_{r_i}}/{W_g}^{1/3}$ used for the calculations of the individual openings, with weights denoted as w_i. The logarithmic weighted average and the weights can be calculated as:

$$\log_{10}\left(\frac{\overline{i_r}}{\sqrt[3]{W_g}}\right) = \frac{\sum \log_{10}\left(\frac{\overline{i_{r_i}}}{\sqrt[3]{W_g}}\right) w_i}{\sum w_i}, \tag{4.37}$$

$$w_i = \frac{1}{\log_{10}\left(\frac{i_{g,i}}{\sqrt[3]{W_g}}\right)}. \tag{4.38}$$

The substitution of $i_{g,i}$ and $\overline{i_{r_i}}$ into the equation should be performed in units of $psi \cdot ms$. The equivalent charge weight W_g should be in lb. The parameter $\rho_{A,f}/{W_g}^{1/3}$ also exhibits differing values when assessed with various openings. However, its behaviour cannot be represented in logarithmic values since it can be equal to 0. For simplicity, in this thesis is used the weighted average of its actual values, with weights w_i calculated as described earlier in Eq. 4.38. This evaluation should be reasonably accurate for values of ${A_v}/{V_f}^{2/3} \leq 1$ and $\rho_{A,f}/{W_g}^{1/3} \leq 19\ kg^{2/3}/m^2$, and should give conservative results. More complex solution of this problem is above the scope of this thesis.

4.4.3 Application

In the scenario outlined in Chapter 4.1, the method provided in Chapters 4.4.1 and 4.4.2 was used to calculate the gas pressures acting on the confinement structures. Detailed description of calculations performed based on the methods described in Chapters 4.3.1 and 0 are not included here as the similar problem is solved in Chapter 4.3.3.

Firstly, the equivalent charge weight for gas pressures was calculated based on information from UFC [11] – the heat of combustion of TNT is $H^c_{TNT} = 15.4\ MJ/kg$ and of octol 70/30 it is $H^c_{Octol} = 11.6\ MJ/kg$. The TNT equivalent for calculations of gas pressures is then [11]:

$$W_g = \frac{\phi(H^c_{Octol} - H^d_{Octol}) + H^d_{Octol}}{\phi(H^c_{TNT} - H^d_{TNT}) + H^d_{Octol}} W_{EXP} = \frac{1 \cdot (11.6 - 6.7) + 6.7}{1 \cdot (15.4 - 6) + 6} 6.3 = 4.75\ kg, \tag{4.39}$$

where H^d are the detonation heats mentioned already in Chapter 4.2.3 and ϕ is the TNT conversion factor calculated as [11]:

$$\phi = \min(1.25 - 0.078\, W/V_f\,; 1) = \ \min(1.25 - 0.78 \cdot 7/75.6\,; 1) = 1. \tag{4.40}$$

The free air volume of the room can be calculated from the setup geometry to be $V_f = 75.6\ m^3$ (assuming the entire volume is free). The peak gas pressure, corresponding to the value of $W_g/V_f = 0.063\ kg/m^3$, was determined as $P_g = 283\ kPa$ from the Figure 27.

Subsequently, the gas impulse considering only the frangible opening *O1* - $i_{g,1}$ was derived following steps C2), C3), and D1) to D3). In this instance, the opening's area is $A_{v,1} = 11.4\ m^2$, resulting in the input $A_{v,1}/{V_f}^{2/3} = 0.64$. The scaled area density of the frangible cover is $\rho_{A,f,1}/W_g^{1/3} = 11.9\ kg^{2/3}/m^2$ (for detailed inputs, refer to Chapter 4.3.3). The impulse $\overline{i_r}$ acting on the frangible element, assuming its intact condition, was determined by the procedure outlined in Chapter 4.3.1, (steps A1) to A3)). The opening *O2* was considered as non-uniformity of the wall *W4*. The resulting average impulse is $\overline{i_r} = 1.33\ MPa \cdot ms$. This value was then used to determine the fictitious scaled distance $Z_{fic} = 0.87\ m/kg^{1/3}$ from Figure 4. With this Z_{fic} value and the scaled area density $\rho_{A,f,1}/W^{1/6} = 14.5\ kg^{5/6}/m^2$ the reflection factor $f_r = 0.87$ was read from the Figure 16. According to D3) the impulse acting on the frangible element was calculated as $\overline{i_{r_1}} = \overline{i_{r_{fr}}} = 1.15\ MPa \cdot ms$. Therefore, the final input parameter for the gas impulse graph reading is $\overline{i_{r_1}}/W_g^{1/3} = 0.69\ MPa \cdot ms/kg^{1/3}$. The resulting gas impulse, considering only opening *O1*, obtained through graph readings (see Figure 28) and logarithmic interpolations, is $i_{g,1} = 4.96\ MPa \cdot \boldsymbol{ms}$.

The gas impulse, considering only the frangible opening *O2* - $i_{g,2}$ was obtained in a similar manner. In this instance, $A_{v,2} = 2.1\ m^2$ → ${A_{v,2}}/{V_f}^{2/3} = 0.23$. As opening *O2* has no cover $\rho_{A,f,2}/W_g^{1/3} = 0\ kg^{2/3}/m^2$. The calculation of $\overline{i_r}$ (for step C2)) closely follows the approach outlined in Chapter 4.3.3. In this case, the influence of the frangible wall is negligible since the intermediate results show $\overline{i_{r_{without}}} \cong \overline{i_{r_{with}}} = 1.77\ MPa \cdot ms$. The input is then $\overline{i_{r_2}}/W_g^{1/3} = 1.05\ MPa \cdot ms/kg^{1/3}$. The resulting gas impulse, considering only *O2*, is $i_{g,2} = 10.76\ MPa \cdot \boldsymbol{ms}$.

Next, the weights w_1 and w_2 have been calculated using Eq. 4.38, which gave $w_1 = 0.397$ and $w_2 = 0.35$. The graph $i_g/W^{1/3}$ to ${A_v}/{V_f}^{2/3}$ was then constructed

through logarithmic interpolation of digitalized UFC 3-340-02 graphs for W_g/V_f (calculated earlier) and for the newly calculated intermediate inputs:

$$\frac{\overline{i_r}}{\sqrt[3]{W_g}} = 10^{\frac{\log_{10}\left(\frac{167}{\sqrt[3]{10.5}}\right)0.397+\log_{10}\left(\frac{256}{\sqrt[3]{10.6}}\right)0.350}{0.397+0.350}} = 93.4\ \frac{psi\cdot ms}{\sqrt[3]{lb}} = 0.84\frac{MPa\cdot ms}{\sqrt[3]{kg}}, \tag{4.41}$$

$$\frac{\rho_{A,f}}{\sqrt[3]{W_g}} = \frac{\frac{\rho_{A,f,1}}{\sqrt[3]{W_g}}w_1 + \frac{\rho_{A,f,2}}{\sqrt[3]{W_g}}w_2}{w_1+w_2} = \frac{11.9\cdot 0.397 + 0\cdot 0.350}{0.397+0.350} = 6.32\ \frac{kg^{2/3}}{m^2}. \tag{4.42}$$

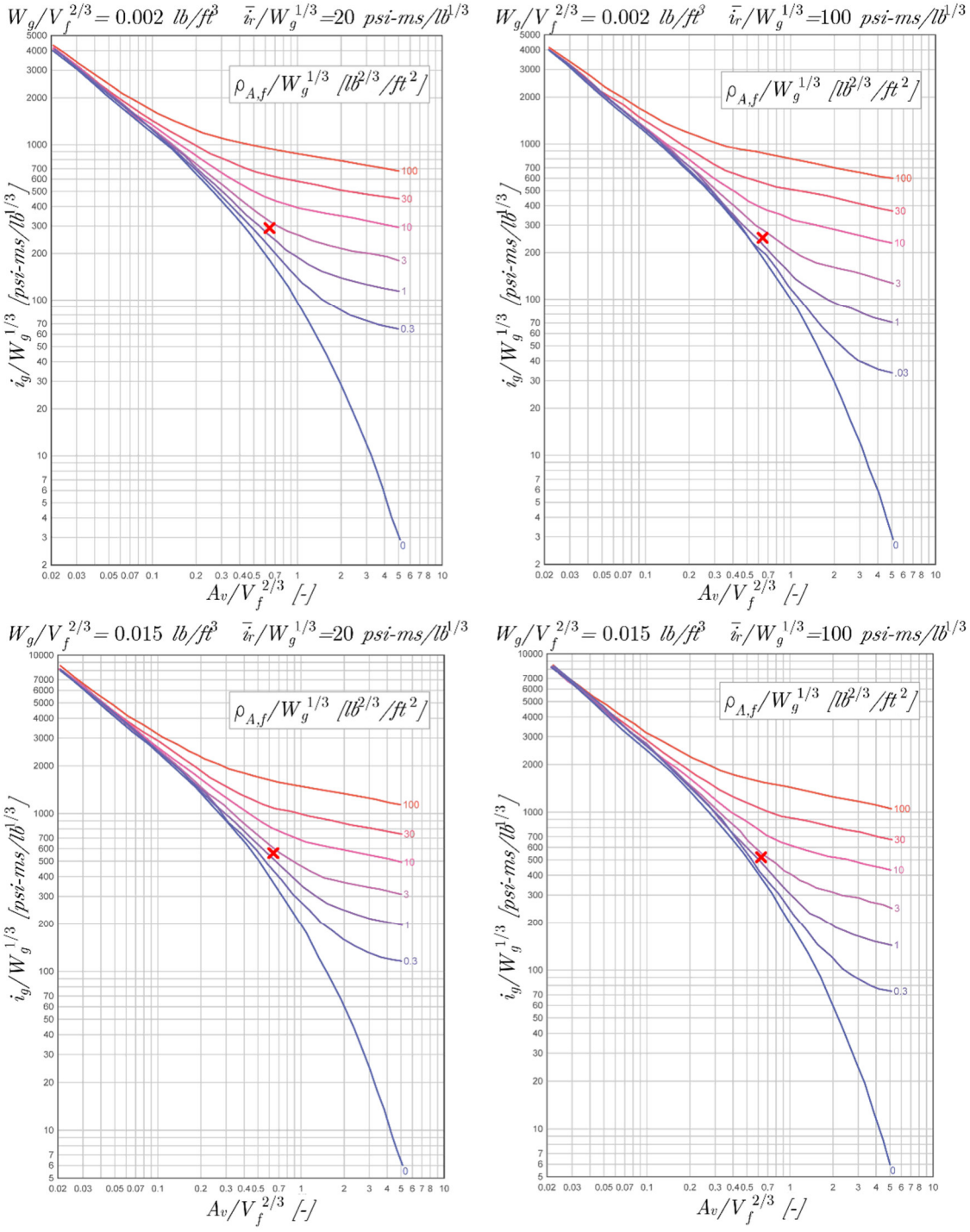

Figure 28: Gas impulse graphs readings

Equation 4.41 is derived from Eq. 4.37 and the substituted values represent the relevant quantities in imperial units. The readings of fictitious scaled areas from the $i_g/W^{1/3}$ to $A_v/{V_f}^{2/3}$ graph are as follows: $A_{v,1,fic}/{V_f}^{2/3} = 0.581$ and $A_{v,2,fic}/{V_f}^{2/3} = 0.256$. Finally, the gas impulse was extracted from the same graph for the value $A_{v,fic}/{V_f}^{2/3} = 0.837$ representing the cumulative sum of the fictitious scaled areas $A_{v,1,fic}/{V_f}^{2/3}$ and $A_{v,2,fic}/{V_f}^{2/3}$. The resulting gas impulse is then $i_g = 3.58\ MPa \cdot ms$. The graph with annotated readings is depicted in Figure 29.

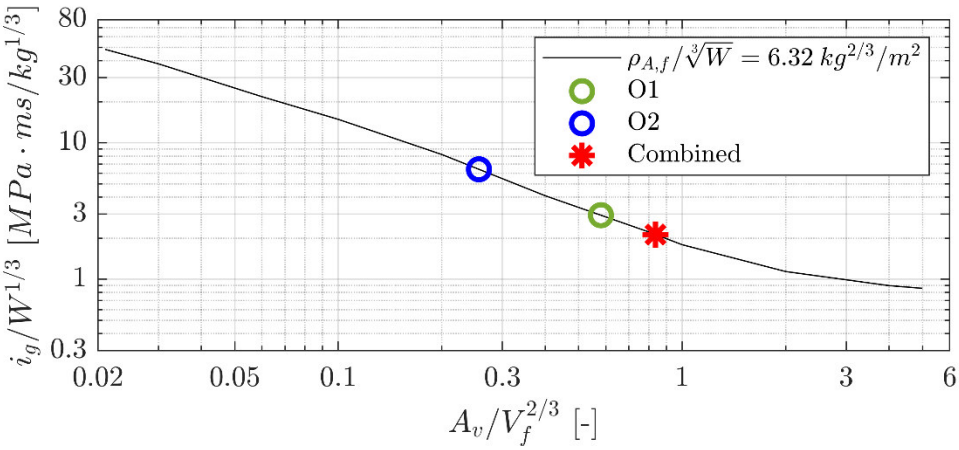

Figure 29: Interpolated $i_g/W^{1/3}$ to $A_v/{V_f}^{2/3}$ graph

The fictitious duration of the gas pressures was calculated using Eq. 2.4 as $t_g = 25.3\ ms$. This duration is greater than the fictitious duration of the blast loads $\bar{t_r}$ (calculated in Chapter 4.3.3), therefore it cannot be neglected, and the confinement is considered to be partially vented.

4.5 Response to Pressures form Confined Explosions

This chapter introduces a simplified calculation method for evaluating the response of two-way simply supported reinforced concrete slab subjected to blast loading, where the Newmark generalised-alpha method is applied for the dynamic calculation. However, this method has been extended for this application to take into account the non-linear behaviour of reinforced concrete. The problem is solved as a system with a single degree of freedom. The methodology is based on the principles outlined in Chapter 2, particularly in chapter 2.4.2.

Chapter 4.5.1 addresses the non-linear behaviour of reinforced concrete slabs. The objective of this section is to determine the resisting forces of a slab structure for a given deflection at its centre. This evaluation is crucial for the

dynamic calculation examined in Chapter 4.5.2. The proposed approach is subsequently applicated on the case study presented in Chapter 4.1.

4.5.1 Reinforced Concrete Slab Behaviour

As previously stated, this chapter aims to assess the restoring force S, which counters the static load for the deflection u at the slab's centre. The method is suitable for two-way simply supported reinforced concrete slabs. The deformation caused by shear forces is neglected in this method. The technique is schematically shown in Figure 30.

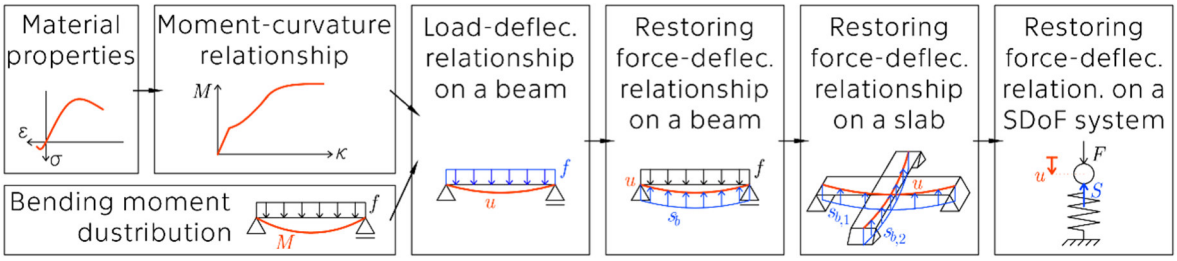

Figure 30: Obtaining the restoring force-deflection relationship of a slab

The stress-strain behaviour of the reinforcement and concrete is considered as shown in Figure 31.

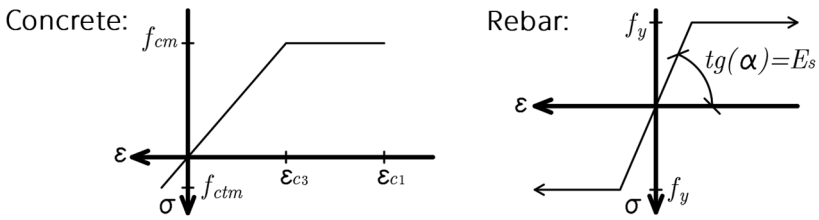

Figure 31: Considered behaviour of concrete and its reinforcement

To obtain the moment-curvature relationship, the procedure for calculating the limit state of serviceability from Eurocode 2-1 is used and extended to include the effects of concrete crushing and reinforcement exceeding its yield strength in tension. The following equation is taken from this norm [23]:

$$\kappa = M[(1-\zeta)C_I + \zeta C_{II}], \tag{4.43}$$

where for any given point on the structure, κ is the curvature, M is the bending moment, C_I is the bending flexibility calculated for the uncracked conditions, C_{II} is the bending flexibility calculated for the fully cracked conditions, and ζ is the distribution coefficient calculated for a case of pure bending according to the following equation [23]:

$$\zeta = \max\left(1 - \beta\left(\frac{M_{cr}}{M}\right)^2; 0\right), \tag{4.44}$$

where $\beta = 1$ for short-term loading and M_{cr} represents the bending moment which causes initial cracking. The parameter C_I can be determined as $C_I = (E_c I_{y,i})^{-1}$, where E_c is the Young's modulus of the concrete and $I_{y,i}$ is the moment of inertia of an ideal section. $I_{y,i}$ can be determined with knowledge of the concrete compression block depth x_c, which can be obtained from the equilibrium of the first moments of area on an ideal section. The value of the parameter C_{II} depends on the nonlinearity of the materials. It can be evaluated using the following equation:

$$C_{II} = \frac{\varepsilon_t + \varepsilon_b}{h_s} \cdot \frac{1}{M}, \tag{4.45}$$

where ε_t represents the strain at the top surface of the slab, ε_b at the bottom surface, and h_s denotes the height of the slab. The behaviour of concrete is simplified by assuming that it acts in tension until the first crack is formed, after which the concrete in tension only affects the performance of the cross-section via distribution coefficient ζ.

In this thesis, a programmed calculation was used to evaluate the moment-curvature relationship. For a given strain at the top surface $\varepsilon_{t,i}$, the program calculates the depths of the concrete compression block x_c for all possible combinations of the behaviour of individual parts of the cross-section. These behaviours include whether the concrete acts in tension or not, whether it is plasticized or not, and whether the reinforcement is plasticized or not. The calculation of x_c for each combination is derived from the equilibrium of forces on the cross-section. Then the conditions for the assumed behaviour in each combination are examined. If met, the moment M of the forces on the cross-section is calculated, and Equations 4.43 to 4.45 are applied. The deformations in the reinforcement and at the bottom surface can be determined, with use of similar triangles, utilizing the values of x_c and $\varepsilon_{t,i}$. This process is executed for $\varepsilon_{t,i} \in \langle \varepsilon_{t,step}; \varepsilon_{c,1} \rangle$, where $\varepsilon_{t,i+1} = \varepsilon_{t,i} + \varepsilon_{t,step}$. The parameter $\varepsilon_{t,step}$ is the value chosen by the user to modify the accuracy of the method. The result is a series of points plotted on a κ to M graph, with linear interpolation available for points in between.

The load-deflection relationship of a statically determined beam can be obtained by a simplified procedure. The beam is divided into finite sections. The section i has a length L_{step} and a constant approximal curvature κ_i read for value

of M calculated for its centre from the a κ to M graph created earlier. At the ends of the beam and at the boundaries between neighbouring sections, two unknown quantities can be defined - deflection $u_{i,i+1}$ and rotation $\varphi_{i,i+1}$, some of which can be defined by boundary conditions. For segment i, the unknown quantities on both sides are linked by the following relations (the notations are explained in Figure 32):

$$u_{i,i+1} = u_{i-1,i} - \varphi_{i-1,i} L_{step} - \frac{\kappa_i {L_{step}}^2}{2}, \tag{4.46}$$

$$\varphi_{i,i+1} = \varphi_{i-1,i} + \kappa_i L_{step}. \tag{4.47}$$

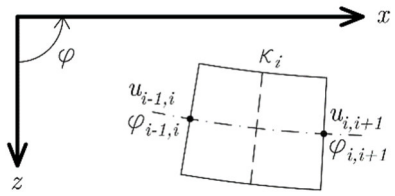

Figure 32: Load-deflection dependency – notation

This leads to a series of equations from which the unknowns can be determined. The beam's deformation at its centre u can then be evaluated easily. The program computes these calculations for various uniform line loads $f_{x,j} \in \langle f_{x,step}; f_{x,max} \rangle$, where $f_{x,j+1} = f_{x,j} + f_{x,step}$. The limiting value $f_{x,max}$ corresponds to the load that creates maximal load-bearing moment on the structure. The results are stored as points on the f_x to u diagram, with a linear approximation between them, similar to the moment-curvature relationship. The user's selected value of L_{step} affects the precision of this calculation, while f_{step} controls the density of the points on the diagram.

Given that the restoring force per unit area of a beam, denoted as s_b, is, in statics, equal to the loading force acting upon it, it can be stated that $s_b(u(f)) = f$. The restoring force per unit area of a two-way slab, denoted as s, can be determined as the superposition of the area restoring forces of two unit-width strips oriented perpendicular to each other, resulting in $s(u) = s_{b,x}(u) + s_{b,y}(u)$. It is worth noting that this approach does not account for the lifting of the corners of the slab.

Lastly, the relationship between the condensed restoring force S and acting on the condensed mass representing the slab, and the deflection at the centre of the slab u can be derived as follows: $S(u) = s(u) \cdot A$, where A represents the area of the slab.

4.5.2 Newmark Generalized-Alpha

The application of the Newmark G-α (Generalized-alpha) method to Eq. 2.7 results in the following balance equation for a single degree of freedom system (the notation is shown in Figure 33) [26]:

$$m\ddot{u}_{i+1-\alpha_m} + C\dot{u}_{i+1-\alpha_f} + S_{i+1-\alpha_f} = F_{i+1-\alpha_f}. \tag{4.48}$$

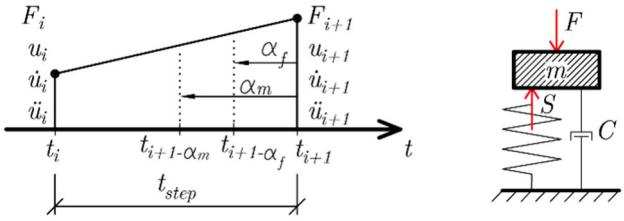

Figure 33: Newmark G-α notation

For the purpose of this thesis, the damping of the system represented by $C\dot{u}$ has been neglected. To read intermediate values of all required quantities (for $t_{i+1-\alpha_m}$ and $t_{i+1-\alpha_f}$), it is recommended to use linear interpolation - refer to the following equations [27]:

$$\ddot{u}_{i+1-\alpha_m} = (1-\alpha_m)\ddot{u}_{i+1} + \alpha_m\ddot{u}_i, \tag{4.49}$$

$$S_{i+1-\alpha_f} = (1-\alpha_f)\ S_{i+1}(u_{i+1}) + \alpha_f\ S_i(u_i), \tag{4.50}$$

$$F_{i+1-\alpha_f} = (1-\alpha_f)F_{i+1} + \alpha_f F_i. \tag{4.51}$$

This method also exploits the Newmark approximations - see the following equations [28]:

$$u_{i+1} = u_i + \dot{u}_i t_{step} + \left(\frac{1}{2} - \beta\right)\ddot{u}_i {t_{step}}^2 + \beta\ \ddot{u}_{i+1} {t_{step}}^2, \tag{4.52}$$

$$\dot{u}_{i+1} = \dot{u}_i + (1+\gamma)\ddot{u}_i t_{step} + \gamma\ \ddot{u}_{i+1} t_{step}. \tag{4.53}$$

The user chosen parameters $\alpha_f, \alpha_m, \beta, \gamma \in \langle 0;1\rangle$ determine the convergence and stability of the method, and the numerical damping. The numerical damping can be expressed by a single variable $\rho_\infty \in \langle 0;1\rangle$, from which all other parameters can be derived – see the following equations [26]:

$$\alpha_f = \frac{\rho_\infty}{\rho_\infty + 1}, \tag{4.54}$$

$$\alpha_m = \frac{2\rho_\infty - 1}{\rho_\infty + 1}, \tag{4.55}$$

$$\beta = \frac{1}{4}(1 - \alpha_m + \alpha_f)^2, \tag{4.56}$$

$$\gamma = \frac{1}{2} - \alpha_m + \alpha_f. \tag{4.57}$$

If $\ddot{u}_{i+1}$ is expressed from Eq. 4.52 and substituted it along with equations 4.49, to 4.51 into Eq. 4.48, and then from it u_{i+1} is expressed, it results in the following equation (without considering damping):

$$u_{i+1} = \frac{m\left[\frac{1-\alpha_m}{\beta}\left(\frac{u_i}{{t_{step}}^2}+\frac{\dot{u}_i}{t_{step}}+\frac{\ddot{u}_i}{2}\right)-\ddot{u}_i\right]+(1-\alpha_f)(F_{i+1}-S_{i+1})+\alpha_f(F_i-S_i)}{m\frac{1-\alpha_m}{\beta\ {t_{step}}^2}}. \quad (4.58)$$

However, in this equation the u_{i+1} is needed for calculation of S_{i+1}, but due to the non-linear behaviour of the structure, it cannot be expressed from it. In this thesis, this problem is solved by iterative computation. For each calculation of u_{i+1} the value S_{i+1} is initially guessed as $S_{i+1} = S_i$, then Eq. 4.58 is utilised to obtain the approximate value of u_{i+1}. The deflection at the end of the time-step is used for improved evaluation of S_{i+1}, which can be utilised further for a more precise assessment of u_{i+1}. This cycle continues until the residue of the balance equation 4.48 is not smaller than the limiting user chosen value $F_{res,lim}$.

For a 1D problem, the evaluation of mass m can be done by finding the length L_1, that with global deformation u has the same area under the deflection curve as the actual structure (defining function of deflection is denoted as $f_u(x)$). For a simply supported beam, this results in the following equation (see Figure 34 for notation):

$$\int_0^L f_u(x)dx = L_1\ f_u(L/2\ ). \quad (4.59)$$

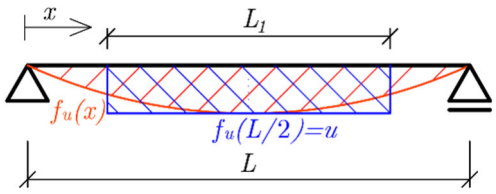

Figure 34: Determination of condensed mass on simply supported beam

For a slab, this length can be calculated for both spans and the mass m is then calculated as the multiplication of those lengths and the area density of the slab. In the calculation of m performed in this thesis the effect of nonlinear behaviour of the slab is neglected. For a simply supported beam and constant loading force this leads to $L_1 = 0.64\,L$.

The approach presented in this chapter can only be used in combination with the outputs of Chapter 4.5.1 until the maximal deflection u_{max} is reached, as the behaviour of the structure is not defined for a load removal. This problem is

beyond the scope of this thesis. Additionally, if the ultimate load-bearing moment is exceeded, the subsequent deformation can no longer be described by this procedure.

4.5.3 Application

The following section analyses the response of wall *W2* (refer to Figure 11), taken from the case study in Chapter 4.1, to illustrate the application of the method discussed in Chapters 4.5.1 and 4.5.2. It is assumed that the wall *W2* is not significantly loaded in its plane and the stress caused by these loads can be neglected - the wall is only stressed by the bending moment caused by the explosive event. Therefore, the application of the method is viable.

The inputs for the programmed approach included the geometrical properties of the wall and its reinforcement, material properties obtained from EC-2-1 ($\varepsilon_{c1} = 3.5$ ‰, $\varepsilon_{c3} = 1.75$ ‰, $E_s = 200\ GPa$, $f_{ctm} = 2.565\ MPa$ [23] – refer to Figure 31), and the parameters of Newmark G-α defined by $\rho_\infty = 1$ (no numerical damping). The time step length was set as $t_{step} = 0.1\ ms$, and the loading $P(t)$ was determined by selecting the higher value between blast pressures and gas pressures (calculated in Chapters 4.3.3 and 4.4.3, respectively) at a given time instant.

The computed moment-curvature relationship of a vertical 1 m wide strip of wall *W2* is presented in Figure 35 a). The precision used for the computation was determined by $\varepsilon_{t,step} = \varepsilon_{c1}/500$. In the mentioned graph, it can be observed that, due to the low reinforcement of the concrete wall, the tension reinforcement almost instantaneously plasticizes after the concrete in tension starts cracking. Both strips were divided into 50 elements, and their load-deflection relationships were computed. This relationship of the vertical strip is illustrated in Figure 35 b).

The result of the Newmark G-α dynamic analysis is shown in Figure 36. From the shown graphs, it can be concluded that wall *W2*, after loading, would likely remain intact; however, it will be severely damaged – the tension reinforcement in both directions will exceed its yield strain, and the compressed concrete will be crushed.

This computation likely yields conservative results - computed deformations are probably higher than they would likely to be in reality. The prestress caused by the wall's own weight is not considered. Considering the geometry of the

setup, the supports of the wall should be treated as fixed or partially fixed. Despite the formation of a plastic hinge around the edges, this will result in a stiffer behaviour of the wall in the early stages of the response. Additionally, the effect of corners being held down contributes to lowering the overall response. Nevertheless, this calculation and its results can serve as the basis for a 'first-cut' estimate of the response.

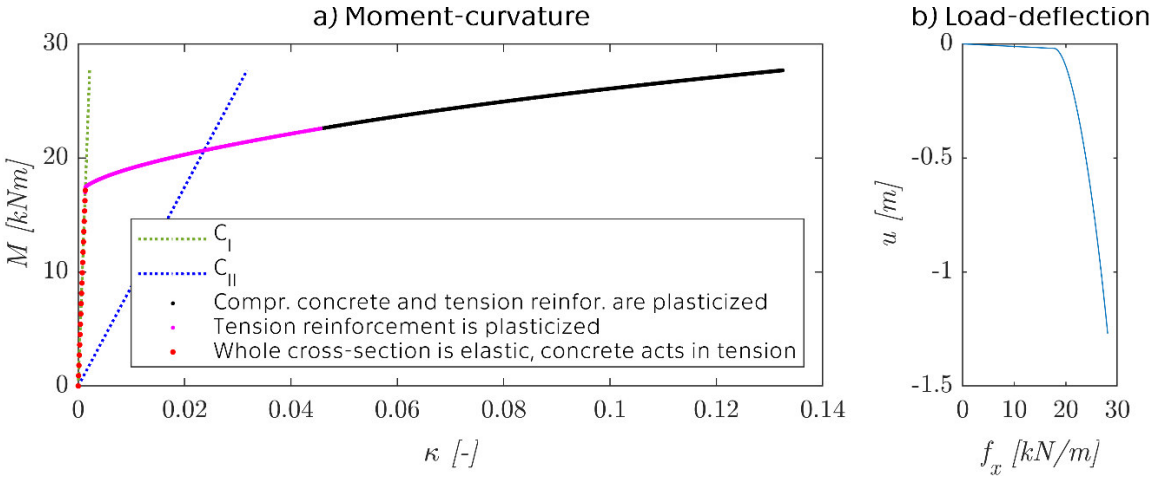

Figure 35: Computed realtionships of the vertical strip

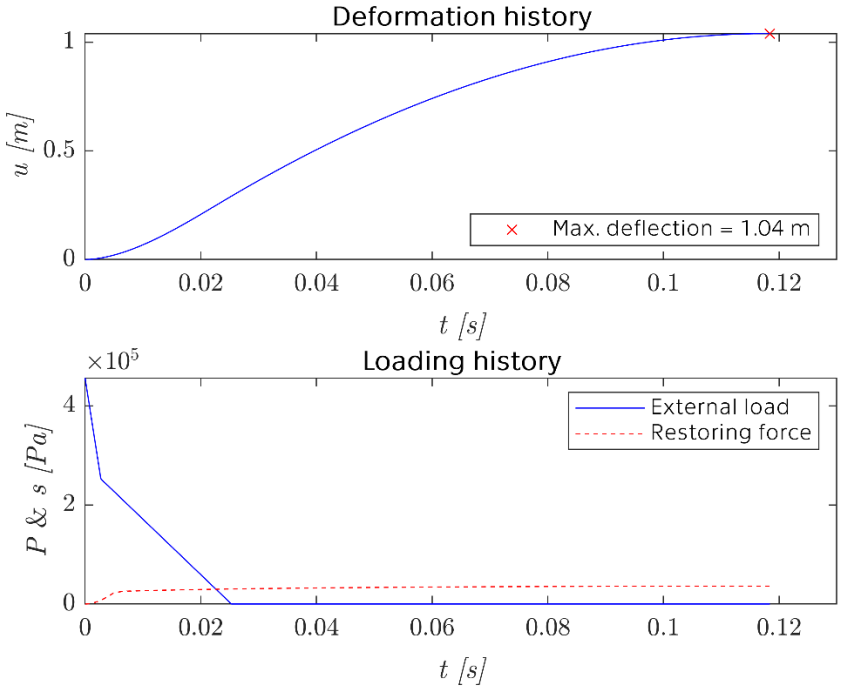

Figure 36: Results of Newmark G-α dynamic analysis

5 Conclusion

Limitations of the blast load assessment methods described in NUREG/CR-0442 (for close-in explosions) and UFC 3-340-02 (for confined explosions) were identified. Through extensions of those methods this thesis evaluates the structural response of reinforced concrete structures subjected to close-in explosion that have supports relatively close to the mostly loaded section of the structure, and structures subjected to the confined explosions for confinements with fragile frangible elements and multiple vent openings.

The approach outlined in NUREG/CR-0442 was implemented into a computer program to determine the plastic hinge radius of a wall segment. A method for assessing the reduction of reflected blast pressures from fragmented frangible elements was developed by tracking the time evolution of additional venting area created between the fragments. The evaluation procedure for gas pressure duration in confined spaces with multiple openings, addressed in Chapter 4.4.2, focused on medium-sized openings $(A_v/{V_f}^{2/3} \leq 1)$ with light covers $(\rho_{A,f}/W_g^{1/3} \leq 19\ kg^{2/3}/m^2)$. Chapter 4.5 explains a simple method for determining the response of simply supported reinforced concrete slab structures to blast loading. The method uses the Newmark G-α method, adapted to consider the non-linear behaviour of reinforced concrete structures.

All the mentioned methods were applied to a complex case study involving the exposure of a medium-sized room within a reinforced concrete structure to a 6.3 kg Octol 70/30 explosive. The analysis suggests that the load-bearing structures confining the room would be severely damaged and partially disintegrated from this explosive event. Furthermore, the analysis of the blast wave reflection from the frangible element indicates that the effect of its fragmentation has, in this case, a negligible influence.

The theoretical framework presented in this thesis provides a foundation for future studies to build upon. The method for evaluating the reduction of reflected blast pressures from fragmented frangible elements could benefit from additional support or refinement through physical or numerical experiments. Furthermore, the calculation of the effect of multiple openings on the gas impulse has the potential for extension to consider heavier covers or larger openings.

Bibliography

[1] DASEY, Jason. The frightening moment a missile hit a Kyiv apartment building, attacking Ukraine's 'splendid, peaceful' capital. *ABC News*. Online. c2023. [Accessed 25 September 2023]. Retrieved from: https://www.abc.net.au/news/2022-02-26/frightening-moment-a-missile-hit-a-residential-building-in-kyiv/100864932

[2] Residential building in Kiev hit by air defense missile - Russian Defense Ministry source. *TASS*. Online. [2022]. [Accessed 25 September 2023]. Retrieved from: https://tass.com/defense/1411853

[3] Fake: Ukrainian Missile Destroys Apartment Building in Kyiv. *Stop fake*. Online. [2022]. [Accessed 25 September 2023]. Retrieved from: https://www.stopfake.org/en/fake-ukrainian-missile-destroys-apartment-building-in-kyiv/

[4] MAKOVIČKA, Daniel, JANOVSKÝ, Břetislav and ČERNÍN, Milan. *Příručka protivýbuchové ochrany staveb*. Online. Praha: Česká technika - nakladatelství ČVUT v Praze, 2008. [Accessed 19 September 2023]. ISBN 978-80-01-04090-4. Retrieved from: http://www.makovicka.cz/data/S/U/t/2008-pvoch-cz.pdf

[5] TATALÁK, Adam. *Deformačně-napěťová analýza tenkostěnné skříně vystavené rázovému zatížení od výbuchu*. Online. Master's thesis. Brno, 2016. [Accessed 19 September 2023]. Retrieved from: https://dspace.vutbr.cz/bitstream/handle/11012/59564/final-thesis.pdf?sequence=-1&isAllowed=y

[6] SHERKAR, Pushkaraj, WHITTAKER, Andrew and AREF, Amjad. *Modeling the effects of detonations of high explosives to inform blast-resistant design*. Online. University at Buffalo, State University of New York, 2010. [Accessed 19 September 2023]. Retrieved from: https://www.researchgate.net/publication/269875941_Modeling_the_effects_of_detonations_of_high_explosives_to_inform_blast-resistant_design

[7] VRBA, Pavel. *Základy problematiky výbuchu a jejich vliv na stavební konstrukce.* Online. CTU in Prague, 2020. [Accessed 19 September 2023]. Retrieved from: https://concrete.fsv.cvut.cz/phdworkshop/proceedings/2020/pdf/Vrba_Pavel.pdf

[8] SCOTT, Tom and MILLER, Steve. "High explosives" doesn't just mean "bigger boom." *YouTube*. Online. 2021. [Accessed 19 September 2023]. Retrieved from: https://www.youtube.com/watch?v=OOWcTV2nEkU&ab_channel=TomScott

[9] RIGBY, S.E., OSBORNE, C., LANGDON, G.S., COOKE, S.B. and POPE, D.J. Spherical equivalence of cylindrical explosives: Effect of charge shape on deflection of blast-loaded plates: Effect of charge shape on deflection of blast-loaded plates. *International Journal of Impact Engineering*. Online. 2021. Vol. 155. [Accessed 19 September 2023]. ISSN 0734-743X. Retrieved from: https://www.sciencedirect.com/science/article/abs/pii/S0734743X21000798?via%3Dihub

[10] SIMOENS, Bart and LEFEBVRE, Michel. Influence of the Shape of an Explosive Charge: Quantification of the Modification of the Pressure Field: Quantification of the Modification of the Pressure Field. *Central European Journal of Energetic Materials*. Online. 2015. Vol. 12, p. 195-213. [Accessed 19 September 2023]. Retrieved from: https://www.infona.pl/resource/bwmeta1.element.baztech-4fd4d478-9d50-47f4-b1ac-dac04fd399dc/content/partDownload/71f22992-5cf7-3b59-af73-bb333ec76e66

[11] *UFC 3-340-02 Structures to Resist the Effects of Accidental Explosions*. Online. U.S. Army Corps of Engineers, 2008. [Accessed 19 September 2023]. Retrieved from: https://www.wbdg.org/FFC/DOD/UFC/ARCHIVES/ufc_3_340_02.pdf

[12] KARLOS, Vasilis, VIACCOZ, Bernard and SOLOMOS, George. *Calculation of blast loads for application to structural components*. Online. Publications Office, 2013. [Accessed 19 September 2023]. ISBN 978-92-79-35158-7. Retrieved from: https://op.europa.eu/en/publication-detail/-/publication/5f38f443-0e1b-4e41-a30e-0f89d22863f2

[13] RAMAMURTHI, Krishnaswami. Mod-01 Lec-01 Loud Bang and Disruption. *YouTube*. Online. 2014. [Accessed 19 September 2023]. Retrieved from: https://www.youtube.com/watch?v=NKqdLj5fR1o&ab_channel=nptelhrd

[14] KARLOS, Vasileios, SOLOMOS, George and LARCHER, Martin. *Analysis of blast parameters in the near-field for spherical free-air explosions*. Online. Publications Office of the European Union, 2016. [Accessed 19 September 2023]. ISBN 978-92-79-57603-4. Retrieved from: https://publications.jrc.ec.europa.eu/repository/handle/JRC101039

[15] SCHAUFELBERGER, Benjamin, ROLLER, Christoph and RIEDEL, Werner. *Scaling Rules for the Analysis of Blast Loaded Concrete Structures – a Critical Literature Review*. Online. 2017. [Accessed 19 September 2023]. Retrieved from: https://publica-rest.fraunhofer.de/server/api/core/bitstreams/4930824b-afeb-4832-9834-d89a0faf4bc5/content

[16] KEENAN, W.A. and TANCRETO, J.E. *Blast Environment from Fully and Partially Vented Explosions in Cubicles*. Online. Civil Engineering Laboratory, Naval Construction Battalion Center, 1975. [Accessed 19 September 2023]. Retrieved from: https://apps.dtic.mil/sti/citations/ADA019026

[17] REMENNIKOV, M. Alex. *The state of the art of explosive loads characterisation*. Online. University of Wollongong, 2007. [Accessed 19 September 2023]. Retrieved from: https://aees.org.au/wp-content/uploads/2013/11/07-Remenikov-Alex.pdf

[18] The Mach Stem. *Atomic archive*. Online. c1998-2023. [Accessed 19 September 2023]. Retrieved from: https://www.atomicarchive.com/science/effects/mach-stem.html

[19] LI, Xing-long, WANG, Xiang, LU, Zhong-hua, LI, Ming, CAO, Wei, CHEN, Ke-quan, XUE, Peng-yi, HUANG, Heng-jian, HUA, Cheng and GAO, Da-yuan. Numerical simulations of trajectories of shock wave triple points in near-ground explosions of TNT charges. *Energetic Materials Frontiers*. Online. 2022. Vol. 3, no. 2p. 61-67. [Accessed 27 October 2023]. DOI https://doi.org/10.1016/j.enmf.2022.02.001.

[20] KOT, C.A., VALENTIN, R.A., MCLENNAN, D.A. and TURULA, P. *Nureg/CR-0442: Effects of air blast on power plant structures and components*. Online. Argonne National Lab., IL (USA), 1978. [Accessed 19 September 2023]. Retrieved from:

https://inis.iaea.org/collection/NCLCollectionStore/__Public/10/448/10448846.pdf?r=1

[21] ERLICHER, Silvano, BONAVENTURA, Luca and BURSI, S. Oreste. *The analysis of the Generalized – α methods for non-linear dynamic problems*. Online. Università di Trento, 2001. [Accessed 19 September 2023]. Retrieved from: https://hal.science/hal-00345290/document

[22] MAKOVIČKA, Daniel and MAKOVIČKA, Daniel. BLAST LOAD OF BUILDING STRUCTURE. *Engineering Mechanics*. Online. 2014. Vol. 21., no. 1.p. 11-18. [Accessed 20 September 2023]. Retrieved from: http://www.engineeringmechanics.cz/pdf/21_1_011.pdf

[23] ČSN EN 1992-1-1 ed. 2. *Eurokód 2: Navrhování betonových konstrukcí - Část 1-1: Obecná pravidla a pravidla pro pozemní stavby*. Praha: ÚNMZ, 2019. 2rd ed.

[24] ČSN EN 1992-1-1 NA ed. A. *National Annex - Eurocode 2: Design of concrete structures - Part 1-1: General rules and rules for buildings*. Praha: ÚNMZ, 2020. ed. A

[25] ZHOU, Zhihui, WEN, Ying, CAI, Chenzhi and ZENG, Qingyuan. *Fundamentals of structural dynamics*. Online. Cambridge, MA : Elsevier, [2021]. [Accessed 1 December 2023]. ISBN 978-0-12-823704-5. Retrieved from: https://www.sciencedirect.com/topics/engineering/linear-acceleration-method

[26] JITHENDER, Timothy and TAGIR, Iskhakov. Lecture 4: Generalized-Alpha Method / Newmark Method. *YouTube*. Online. 2021. [Accessed 7 November 2023]. Retrieved from: https://www.youtube.com/watch?v=wUsTSm-DY1g&t=290s&ab_channel=ComputationalDynamics

[27] ERLICHER, Silvano, BONAVENTURA, Luca and BURSI, O. The analysis of the Generalized -A method for non-linear dynamic problems. *Computational Mechanics*. Online. 2002/01/03. Vol. 28, p. 83-104. [Accessed 7 November 2023]. DOI 10.1007/s00466-001-0273-z. Retrieved from: https://www.researchgate.net/publication/226310820_The_analysis_of_the_Generalized_-A_method_for_non-linear_dynamic_problems

[28] NEWMARK, M. Nathan. A Method of Computation for Structural Dynamics. *Journal of the Engineering Mechanics Division*. Online. 1959. Vol. 85, no. 3p. 67-94. DOI 10.1061/JMCEA3.0000098. [Accessed 19 September 2023]. Retrieved from: https://engineering.purdue.edu/~ce573/Documents/Newmark_A%20Method%20of%20Computation%20for%20Structural%20Dynamics.pdf

List of Used Software

Microsoft Office 365 – university licence

AutoCAD 2022 – university licence

MATLAB R2022b – university licence

SMaths Studio – personal free licence